

Inertial migration of a rigid sphere in three-dimensional Poiseuille flow

Kaitlyn Hood^{1,†}, Sungyon Lee² and Marcus Roper¹

¹Department of Mathematics, University of California, Los Angeles, CA 90095, USA

²Department of Mechanical Engineering, Texas A&M University, College Station, TX 77843, USA

(Received 15 December 2013; revised 11 November 2014; accepted 22 December 2014;
first published online 22 January 2015)

Inertial lift forces are exploited within inertial microfluidic devices to position, segregate and sort particles or droplets. However, the forces and their focusing positions can currently only be predicted by numerical simulations, making rational device design very difficult. Here we develop theory for the forces on particles in microchannel geometries. We use numerical experiments to dissect the dominant balances within the Navier–Stokes equations and derive an asymptotic model to predict the lateral force on the particle as a function of particle size. Our asymptotic model is valid for a wide array of particle sizes and Reynolds numbers, and allows us to predict how focusing position depends on particle size.

Key words: low-Reynolds-number flows, microfluidics, particle/fluid flows

1. Introduction

Inertial microfluidic devices employ inertial focusing to segregate and sort chains of particles, and to move particles between streams of different fluids. For example, centrifuges on a chip (Mach *et al.* 2011; Sollier *et al.* 2014) trap circulating cancer cells from blood in microchannel vortices, and sheathless high-throughput flow cytometry (Hur, Tse & Di Carlo 2010; Chung, Gossett & Di Carlo 2013) fractionates particles from a buffer in order to image and count rare blood cells. However, there are no predictive theories that describe the trajectories of particles during inertial focusing. Instead, the features of these devices, including flow rate and geometry, are optimized by experimental trial and error. Although asymptotic theories exist for inertial lift forces, they are quantitatively correct only for asymptotically small particles, much smaller than the particles that are typically used in microfluidic devices. Previous asymptotic theories also do not predict how differently sized particles will be differently focused (Di Carlo *et al.* 2009).

Inertial migration of particles was first observed by Segré & Silberberg (1961). Experiments showed that a dilute suspension of neutrally buoyant particles flowing in a cylindrical pipe at moderate speeds will migrate across streamlines (Segré & Silberberg 1961, 1962*a,b*). Particles initially uniformly dispersed through the cross-section of the pipe became focused into a ring with radius 0.6 times the channel radius. Since the reversibility of the Stokes equations (the limit of the Navier–Stokes

† Email address for correspondence: kaitlyn.t.hood@gmail.com

Study	α	Re	Re_p	p	Comments
Rubinow & Keller (1961)	—	—	$\ll 1$	5	Uniform flow and absence of walls
Saffman (1965)	—	—	$\ll 1$	2	Wall effect: particle lags behind fluid
Cox & Brenner (1968)	$\ll 1$	$\ll 1$	$\ll \alpha^2$	—	Implicit analytic force expression
Ho & Leal (1974)	$\ll 1$	$\ll 1$	$\ll \alpha^2$	4	Two-dimensional geometry
Vasseur & Cox (1976)	$\ll 1$	$\ll 1$	$\ll \alpha^2$	—	Agrees with Ho & Leal away from wall
Cox & Hsu (1977)	$\ll 1$	$\ll 1$	$\ll \alpha^2$	—	Agrees with Ho & Leal near wall
Schonberg & Hinch (1989)	$\ll 1$	$O(1)$	$\ll 1$	4	Matched asymptotics
McLaughlin (1991)	—	—	$\ll 1$	2	Extends Saffman for finite slip velocity
Hogg (1994)	$\ll 1$	$O(1)$	$\ll \alpha$	4	Studies non-neutrally buoyant particles
Asmolov (1999)	$\ll 1$	$O(10^3)$	$\ll 1$	4	Extends Schonberg & Hinch for large Re
Di Carlo <i>et al.</i> (2009)	$O(1)$	$O(10^2)$	$O(10)$	3	Three-dimensional numerics and experiments
This paper	$O(1)$	$O(10^2)$	$O(10)$	—	Reconciles with $\alpha \ll 1$ theory

TABLE 1. A comparison of the parameters α , Re and Re_p , and the value of the exponent p for the scaling law $F \sim \rho U^2 a^p$, for various studies, where ρ is the fluid density, U is the characteristic flow velocity and a is the particle radius.

equations (NSEs) when the Reynolds number $Re = 0$) prohibits movement across streamlines, this migration must arise from inertia in the flow (Bretherton 1962).

Many theoretical studies of this effect using asymptotic theory are described below. Each study focuses on a particular limit of two dimensionless groups, Re and α . The first parameter, Re , is the channel Reynolds number, and depends only on the dimensions of the pipe and the properties of unladen flow into the channel. The second parameter, α , is a ratio of the particle size to a characteristic channel length scale. Some studies take this length scale to be the width of the channel, others the distance between the particle and the wall. Values for these parameters in various studies are compiled in table 1.

Although early theoretical studies (Rubinow & Keller 1961; Saffman 1965) illuminated how inertial lift forces are generated by applied torques or body forces, Cox & Brenner (1968) were the first to directly address lift forces on neutrally buoyant particles. They consider a body of arbitrary shape suspended in a fluid bounded by a system of walls in three dimensions, and observe that viscous stresses dominate over inertial stresses, provided that $Re \ll \alpha$. Assuming rapid flow field decay, i.e. viscous stresses remain dominant over inertial stresses throughout the fluid, they derive an implicit analytic expression for the force by a regular perturbation expansion of the NSEs in the small parameter Re . They show that this assumption is valid for the lateral migration of a sphere in flow through a cylinder with arbitrary cross-section. Subsequently, they arrive at an integral formula for the lift force for a neutrally buoyant sphere, but they do not evaluate the integrals to determine how lift forces vary across the channel, or how they depend on particle size. Additionally,

McLaughlin (1991) extended the theory of Saffman (1965) to non-neutrally buoyant particles by considering a finite slip velocity.

Ho & Leal (1974) were the first to explicitly calculate the lift force on a particle in the presence of channel walls, by developing an asymptotic theory for a particle in two-dimensional (2D) Couette and Poiseuille flows. Since there are multiple scales for the dynamics in the particle–channel system, Ho & Leal introduce the particle Reynolds number $Re_p = \alpha^2 Re$. They observe that, provided $Re_p \ll \alpha^2$, viscous stresses dominate over inertial stresses throughout the fluid-filled domain. They develop a scaling law for the lift force as a function of the particle position by a regular perturbation series expansion in powers of Re_p . Each term in this expansion can be expanded in powers of α . Retaining only leading-order terms, they find that lift force $F_L \sim \rho U_m^2 \alpha^2 a^2$, where ρ is the fluid density, U_m is the maximum velocity of the background flow and a is the particle radius, i.e. that lift force scales with the fourth power of particle diameter.

Later computations by Vasseur & Cox (1976) apply the result of Cox & Brenner (1968) to a spherical particle flowing between two parallel plates. Provided $Re_p \ll \alpha^2$, only the inner expansion is needed to calculate the first term in the expansion for the migration velocity. The migration velocity is computed as a Fourier integral and no definite scaling law for the lift force is derived. However, they compare their numerical results to those of Ho & Leal (1974) and have good agreement, except near the wall. Similarly, by considering a particle near a single wall and using the results of Cox & Brenner (1968), Cox & Hsu (1977) calculate the migration velocity of a particle near the wall. They do not derive a scaling law for the force, but their numerical results compare well to those of Ho & Leal (1974) near the wall.

Although early theory assumed $Re \ll 1$, in inertial microfluidic devices, and in the experiments of Segré & Silberberg (1961), the channel Reynolds number ranges from 1 to 700. The first theory capable of describing migration of particles in these moderate-Reynolds-number flows was developed by Schonberg & Hinch (1989), who assumed small particle size ($\alpha \ll 1$) and particle Reynolds number ($Re_p = \alpha^2 Re \ll 1$), but allowed for Reynolds number $Re = O(1)$. For particles in a 2D Poiseuille flow, they separate the flow field into inner and outer regions. In the inner region, at distances $O(a)$ from the particle, the viscous stresses are dominant. In the outer region, at distances $a/Re_p^{-1/2}$ from the particle, inertial stresses become co-dominant with viscous stresses. In this outer region, the particle's disturbance of the flow field is weak enough to be linearized around the base flow, reducing the NSE to Oseen's linearized equations (Batchelor 1967). Although the authors solve for the inertial migration velocity for a force-free particle, their calculation can readily be adapted to calculate the lift force, and again predicts $F_L \sim \rho U^2 \alpha^2 a^2$; i.e. that lift force scales with the fourth power of particle size. Hogg (1994) extended the analysis of Schonberg & Hinch (1989) to non-neutrally buoyant particles, while Asmolov (1999) extended the theory of Schonberg & Hinch (1989) to large Re .

In inertial microfluidic experiments, particle diameters may not be small compared to the channel width, and particle Reynolds numbers Re_p can reach values of 10–20. To determine lift forces in this experimentally relevant regime, and to consider focusing in three-dimensional (3D) flows, Di Carlo *et al.* (2009) performed finite element simulations for particles in square channels. They varied Reynolds number Re between 20 and 80 and the ratio of particle size to channel size α between 0.05 and 0.2. They find that, unlike circular pipes, which focus particles to an annulus, square channels focus particles to four symmetrically arranged positions. For particles near the channel centre, numerical fitting of the numerical data generates the power

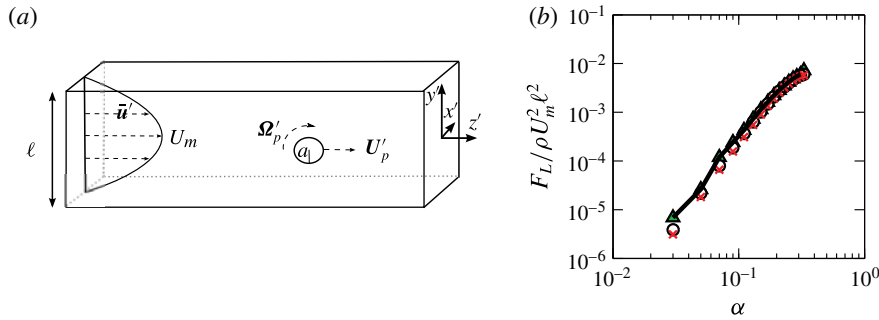


FIGURE 1. (Colour online) (a) The physical system for the flow around a particle suspended in a square channel. (b) Numerical computation of the lift force F_L as a function of particle size α for various Reynolds numbers, $Re = 10$ (triangles), $Re = 50$ (circles) and $Re = 80$ (crosses). The curves collapse when lift force is scaled by $\rho U_m^2 \ell^2$, but the curves are neither a power law with exponent 3 nor exponent 4. A regular perturbation expansion that we computed numerically fits the data extremely well (solid black line).

law $F_L \sim \rho U^2 \alpha a^2$, asserting that the lift force F_L increases with a^3 rather than a^4 . For particles closer to the channel walls, they find different exponents for the scaling of lift force with particle size, depending on particle position. The different exponent in the scaling casts doubt on the use of any of the previous asymptotic theories. Additionally, Di Carlo *et al.* (2009) explore experimentally and numerically how the focusing position of the particle varies with particle size; an observation that is integral to inertial separation devices, but which is not considered in asymptotic theory.

In this paper we explicitly compute the dominant balances in the equations of motion of the particle to show that the asymptotics of Ho & Leal (1974) were essentially correct, and hold for a much larger parameter space of Re and α than the authors realized. Specifically, viscous and pressure stresses dominate over inertial stresses over the entire width of the channel; and the drag force on the particle can be computed by regular perturbation of the equations of slow creeping flow. We perform this regular perturbation analysis to derive asymptotic expressions for the lift force that are quantitatively accurate up to $Re = 80$, and with maximum particle size limited only by the proximity of the walls. Our theory also predicts how focusing position depends on particle radius. We show that the scaling observed by Di Carlo *et al.* (2009) is actually a serendipitous fitting to a perturbation series in α by a single apparent scaling law.

We organize the paper as follows. In § 2 we formulate and solve numerically for the inertial lift force on a drag-free spherical particle, focusing on the dependence of this lift force on particle size and channel Reynolds number. In § 3 we dissect out the dominant balances in these equations. In § 4 we develop a regular perturbation series for the lift force, similar to that of Ho & Leal (1974), and show that it is in quantitatively good agreement with the numerically computed lift force (figure 1b). In § 5 we describe how we generalize the computation to 3D channel flows, and in § 6 we show good agreement of our asymptotic method with experiments and discuss its possible applications.

2. Equations of motion

We model flow through an infinitely long square channel of side length ℓ . A 3D Poiseuille flow $\bar{\mathbf{u}}'$ flowing in the z' -direction is disturbed by a rigid sphere of radius a (figure 1a). Here we use primes to denote dimensional variables. We denote the fluid viscosity by μ , fluid density by ρ and the centre-line velocity of the background flow by U_m . The particle is located at $(x'_0, y'_0, 0)$ and is allowed to translate in the z' -direction with velocity $\mathbf{U}'_p = U'_p \mathbf{e}_{z'}$, and rotate with angular velocity $\boldsymbol{\Omega}'_p$, until it is drag-free and torque-free. The objective of this paper is to calculate the lift forces acting on the particle in the x' - and y' -directions.

There are three important dimensionless parameters: (i) the dimensionless ratio of particle radius to channel diameter $\alpha = a/\ell$, (ii) the channel Reynolds number $Re = U_m \ell / \nu$, and (iii) the particle Reynolds number $Re_p = U_m a^2 / \ell \nu$. Here we write $\nu = \mu / \rho$ for the kinematic viscosity. In common with previous theory (Cox & Brenner 1968; Ho & Leal 1974; Schonberg & Hinch 1989), we will perform dual perturbation expansions in Re_p and α , assuming that both quantities are asymptotically small. In inertial microfluidic experiments (Di Carlo *et al.* 2009), particle diameters may be comparable with the channel dimensions. We will show that our expansions converge even at the moderate values of α accessed in these experiments.

The background flow, $\bar{\mathbf{u}}'$, is square channel Poiseuille flow (Papanastasiou, Georgiou & Alexandrou 1999), and takes the form $\bar{\mathbf{u}}' = \bar{u}'(x', y') \mathbf{e}_{z'}$, where \bar{u}' is defined by

$$\bar{u}'(x', y') = U_m \left[-\frac{1}{2} \left(y'^2 - \left(\frac{\ell}{2a} \right)^2 \right) + \sum_{n=0}^{\infty} \frac{-4\ell^2 (-1)^n \cosh \left(\frac{(2n+1)\pi a x'}{\ell} \right)}{(2n+1)^3 \pi^3 a^2 \cosh \left(\frac{(2n+1)\pi}{2} \right)} \cos \left(\frac{(2n+1)\pi a y'}{\ell} \right) \right]. \quad (2.1)$$

The velocity $\bar{\mathbf{u}}'$ and pressure \bar{p}' solve the Stokes equations with boundary condition $\bar{\mathbf{u}}' = \mathbf{0}$ on the channel walls. We will also need the Taylor series expansion for \bar{u}' around the centre of the particle:

$$\bar{u}'(x', y') = \beta' + \gamma'_x (x' - x'_0) + \gamma'_y (y' - y'_0) + \delta'_{xx} (x' - x'_0)^2 + \delta'_{xy} (x' - x'_0)(y' - y'_0) + \delta'_{yy} (y' - y'_0)^2 + O(r'^3). \quad (2.2)$$

To illustrate the reference frame of the equations we will use later, we first list the dimensionless equations of motion and boundary conditions for the velocity and pressure fields \mathbf{u}'' and p'' expressed in particle-fixed coordinates. We non-dimensionalize these equations by scaling velocities by $U_m a / \ell$, lengths by a and pressures by $\mu U_m / \ell$:

$$\nabla^2 \mathbf{u}'' - \nabla p'' = Re_p [(\mathbf{u}'' + \mathbf{U}_p) \cdot \nabla \mathbf{u}''], \quad (2.3a)$$

$$\nabla \cdot \mathbf{u}'' = 0, \quad (2.3b)$$

$$\mathbf{u}'' = \boldsymbol{\Omega}_p \times \mathbf{r}'' \quad \text{on } r'' = 1, \quad (2.3c)$$

$$\mathbf{u}'' = -\mathbf{U}_p \quad \text{on the walls}, \quad (2.3d)$$

$$\mathbf{u}'' = \bar{\mathbf{u}} - \mathbf{U}_p \quad \text{as } z'' \rightarrow \pm\infty. \quad (2.3e)$$

Now we introduce the disturbance velocity and pressure fields $\mathbf{u} = \mathbf{u}'' - \bar{\mathbf{u}} + \mathbf{U}_p$ and $p = p'' - \bar{p}$, in which the background flow $\bar{\mathbf{u}} - \mathbf{U}_p$ (as measured in this reference frame) is subtracted from \mathbf{u}'' . For reference, the fluid velocity in the laboratory frame is given by $\mathbf{v} = \mathbf{u} + \bar{\mathbf{u}}$. We then obtain the equations of motion and boundary conditions that will be used throughout this paper:

$$\nabla^2 \mathbf{u} - \nabla p = Re_p (\bar{\mathbf{u}} \cdot \nabla \mathbf{u} + \mathbf{u} \cdot \nabla \bar{\mathbf{u}} + \mathbf{u} \cdot \nabla \mathbf{u}), \tag{2.4a}$$

$$\nabla \cdot \mathbf{u} = 0, \tag{2.4b}$$

$$\mathbf{u} = \boldsymbol{\Omega}_p \times \mathbf{r} - \bar{\mathbf{u}} + \mathbf{U}_p \quad \text{on } r = 1, \tag{2.4c}$$

$$\mathbf{u} = \mathbf{0} \quad \text{on the walls,} \tag{2.4d}$$

$$\mathbf{u} = \mathbf{0} \quad \text{as } z \rightarrow \pm\infty. \tag{2.4e}$$

We call the variables that appear in (2.4) the inner variables. Appendix A summarizes the notations used for dimensionless and dimensional variables.

We formulated (2.4) as a finite element model (FEM) with approximately 650 000 linear tetrahedral elements, and solved for \mathbf{u} and p using Comsol Multiphysics (COMSOL, Los Angeles) in a rectangular domain with dimensions $\ell/a \times \ell/a \times 5(\ell/a)$, prescribing \mathbf{u} at the inlet $z = -5(\ell/a)$, and imposing neutral boundary conditions (vanishing stress) at the outlet $z = +5(\ell/a)$. In the FEM, we vary U_p and $\boldsymbol{\Omega}_p$ until there is no drag force or torque on the particle. The FEM Lagrange multipliers, which enforce the velocity boundary condition on the particle, are used to compute the lift force F_L on the drag-free and force-free particle. Bramble (1981) rigorously demonstrates the accuracy of flux calculations from Lagrange multipliers for a Poisson’s equation with Dirichlet boundary conditions. Additionally, we discuss accuracy tests of the FEM discretization for our problem in appendix B.

First, we consider the lift force for particles located on the line of symmetry $x_0 = 0$. Fixing particle position y_0 , we found that curves of lift force F_L against particle size a collapsed for different Reynolds numbers. Particles in different positions have different apparent scalings for F_L as a function of a (figure 5a,b). By assaying a large range of particle sizes α , we see that the empirical fit $F_L \sim \rho U^2 a^3$ observed by Di Carlo *et al.* (2009) is not asymptotic as $a \rightarrow 0$. The data for smallest particle sizes ($\alpha < 0.07$) are consistent with a scaling law of $F_L \sim \rho U^2 a^4 / \ell^2$ as predicted by Ho & Leal (1974) and Schonberg & Hinch (1989), but extrapolation of the asymptotic force law to the moderate particle sizes used in real inertial microfluidic devices ($\alpha \approx 0.1\text{--}0.3$) over-predicts the lift force by more than an order of magnitude.

3. Dominant balances in the equations of motion

The governing equation (2.4) is a balance between momentum flux and the pressure and viscous stresses. Testing the hypothesis that two of these three contributions might form a dominant balance within the equation, we plotted the resultants of the three fluxes as functions of distance from the particle. Specifically, we integrate the ℓ_2 norm of each flux over spherical control surfaces centred at the particle. Let S_r be the boundary of a sphere of radius r centred at the origin, and define the ℓ_2 norm by $\|\mathbf{u}\|_2 = \sqrt{u^2 + v^2 + w^2}$. Then the dimensionless viscous stress resultant acting on the sphere S_r is defined by

$$V(r) = \int_{S_r} \|\nabla \mathbf{u} \cdot \mathbf{n}\|_2 \, ds, \tag{3.1}$$

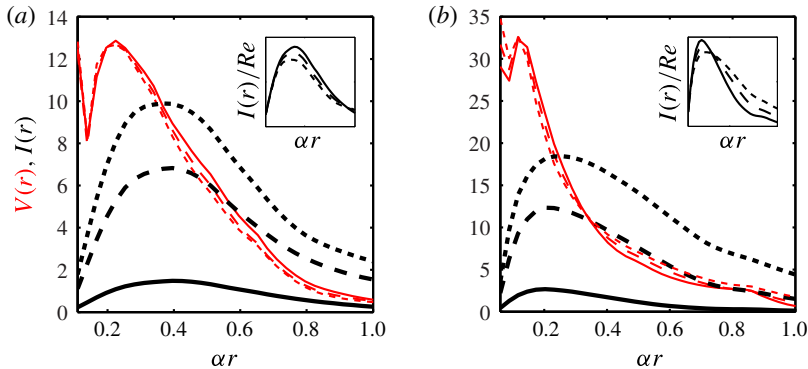


FIGURE 2. (Colour online) The dominant balance of the NSE for (a) a particle near the channel centre ($y_0 = 0.15/\alpha$ and $\alpha = 0.11$) and (b) a particle near the channel walls ($y_0 = 0.35/\alpha$ and $\alpha = 0.06$). The viscous stresses $V(r)$ for various Reynolds numbers are plotted as thin (red) lines, and the inertial stresses $I(r)$ are plotted as thick (black) lines. Reynolds numbers are indicated by line style: $Re = 10$, solid line; $Re = 50$, dashed line; and $Re = 80$, dotted line. The insets show that the inertial stresses $I(r)$ collapse when scaled by Re , suggesting that the high-Reynolds-number dynamics are determined by the low-Reynolds-number dynamics.

and the dimensionless inertial term $I(r)$ stress resultant by

$$I(r) = Re_p \int_{S_r} \|[(\bar{\mathbf{u}} - \mathbf{U}_p)\mathbf{u} + \mathbf{u}(\bar{\mathbf{u}} - \mathbf{U}_p) + \mathbf{u}\mathbf{u}] \cdot \mathbf{n}\|_2 ds. \quad (3.2)$$

The integrand in $I(r)$ is chosen to have divergence equal to the right-hand side of (2.4), and we pick a form of the inertial flux that decays in ℓ_2 norm as $r \rightarrow \infty$.

Numerically evaluating these two terms as well as $(1/r) \int_{S_r} \|\mathbf{p}\mathbf{n}\|_2 ds$, we find that, contrary to the predictions of Ho & Leal (1974) and Schonberg & Hinch (1989), at moderate channel Reynolds numbers, the viscous and pressure stress resultants are numerically larger than the momentum flux. In particular, there is no region in which $V(r)$ and $I(r)$ are co-dominant at $Re = 10$ (figure 2). Indeed, even at higher Reynolds numbers ($Re = 50, 80$) for which inertial stresses are numerically larger than viscous stresses, inertial stresses can be collapsed onto a single curve (see insets of figure 2*a,b*) by rescaling with Re . This scaling suggests that the underlying dynamics, even at moderate values of Re , are inherited from the small- Re dominant balance of pressure and viscous stresses. Dominance of viscous stresses over inertial stresses is surprising because, as Ho & Leal (1974) noticed, the resulting dominant balance equations are not self-consistent for isolated particles in unbounded fluid flow.

We will now present a first-order estimate of the size of the domain in which inertial stresses may be expected to be dominant. The slowest-decaying component of the disturbance flow associated with a force-free particle on the plane of symmetry ($x_0 = 0$) is given by the stresslet flow (Batchelor 1967; Kim & Karrila 2005):

$$\mathbf{u}_{stresslet} = \frac{5\gamma_y(y - y_0)z\mathbf{r}}{2r^5} = O\left(\frac{1}{r^2}\right). \quad (3.3)$$

Cross-over radius αr_*	$y_0 = 0.15/\alpha$ $\alpha = 0.11$			$y_0 = 0.35/\alpha$ $\alpha = 0.06$			
	Re	10	50	80	10	50	80
(i) $\alpha r_* = 1/Re^{1/2}$		0.31	0.14	0.11	0.31	0.14	0.11
(ii) Stresslet with constants (from figure 3)		0.90	0.40	0.30	1	0.30	0.20
(iii) Stresslet with wall effects (from figure 4)		>1	0.45	0.35	>1	0.40	0.30
(iv) NSE with wall effects (from figure 2)		>1	0.60	0.40	>1	0.40	0.30

TABLE 2. The cross-over radius αr_* at which $I(r) \geq V(r)$ computed for $Re = 10, 50, 80$ using the following methods: (i) Ho & Leal’s (1974) calculation using the stresslet, (ii) our calculation using the stresslet, (iii) our calculation using the stresslet and first wall correction, and (iv) our calculation using the numerical solution to the full NSE.

Recall that γ_y is the strain rate, defined in (2.2). For this flow field, the viscous stress term in (2.4) decays with distance like

$$V(r) \sim O(\nabla \mathbf{u}_{stresslet}) \sim O\left(\frac{1}{r^3}\right), \tag{3.4}$$

whereas the inertial stresses vary with distance like

$$I(r) \sim O(Re_p(\mathbf{u}_{stresslet})(\bar{\mathbf{u}} - \mathbf{U}_p)) \sim O\left(\frac{Re_p}{r}\right). \tag{3.5}$$

We define the cross-over radius, r_* , to be the distance at which the viscous and inertial stresses are comparable,

$$r_* = O\left(\frac{1}{Re_p^{1/2}}\right). \tag{3.6}$$

In order to compare the cross-over radius to the width of the channel, we consider when $\alpha r_* = O(1/Re^{1/2})$ is equal to one. To ensure that viscous stresses dominate over inertial stresses over the channel cross-section (i.e. $\alpha r_* \gg 1$), Ho & Leal (1974) restrict to cases where $Re \ll 1$. The asymptotic analysis of Schonberg & Hinch (1989) allows that $Re = O(1)$, but at the cost of needing to separately model and match the flows at $O(1)$ distances from the particle where viscous stresses are dominant, and at $O(1/Re^{1/2})$ distances where inertial and viscous stresses must both be included in the dominant balance.

However, the predicted cross-over radius falls short of the numerical cross-over radius (figure 2, table 2). There are two explanations for the dominance of viscous stresses over inertial in these experimental geometries. First, the above estimates do not consider the coefficients in the stresslet, merely the order of magnitude of the terms. Second, although the stresslet describes the flow disturbance for a force-free particle in an unbounded fluid, the leading-order flow is considerably altered by the presence of the channel walls. Below, we demonstrate that both explanations contribute to the dominance of viscous stresses throughout the channel cross-section, pushing the cross-over radius r^* out beyond the channel walls (table 2).

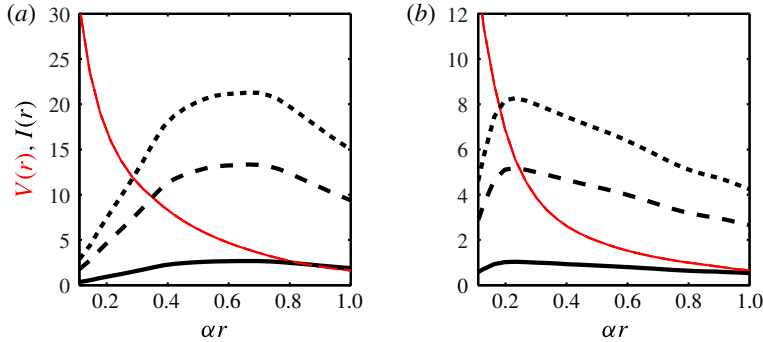


FIGURE 3. (Colour online) The dominant balance that arises from the stresslet approximation of the flow for (a) a particle near the channel centre ($y_0 = 0.15/\alpha$ and $\alpha = 0.11$) and (b) a particle near the channel walls ($y_0 = 0.35/\alpha$ and $\alpha = 0.06$). The viscous stresses $V(r)$ for various Reynolds numbers are plotted as thin (red) lines, and the inertial stresses $I(r)$ are plotted as thick (black) lines. Reynolds numbers are indicated by line style: $Re = 10$, solid line; $Re = 50$, dashed line; and $Re = 80$, dotted line.

3.1. Role of the stresslet constants

We compute $I(r)$ and $V(r)$ numerically for the stresslet flow field (i.e. substitute $\mathbf{u} = \mathbf{u}_{\text{stresslet}}$ in (3.1) and (3.2)). We examine two representative cases: a medium-sized particle near the channel centre ($y_0 = 0.15/\alpha$, $\alpha = 0.11$) (figure 3a), and a small particle near the channel wall ($y_0 = 0.35/\alpha$, $\alpha = 0.06$) (figure 3b). For $Re = 10$, in both cases the inertia is significantly smaller than the viscous stress throughout the channel. At larger values of Re , $I(r)$ eventually exceeds $V(r)$, but the cross-over radius r_* is much larger than simple order-of-magnitude estimates would suggest (table 2).

3.2. Role of wall effects

To estimate how wall modifications of the disturbance flow affect the dominant balances in (2.4), we numerically computed the first wall correction. That is, we substitute $\mathbf{u} = \mathbf{u}_{\text{stresslet}} + \mathbf{u}_{\text{image}}$ into (3.1) and (3.2), where $\mathbf{u}_{\text{image}}$ is a solution of Stokes' equations with boundary condition $\mathbf{u}_{\text{image}} = -\mathbf{u}_{\text{stresslet}}$ on the channel walls. We examine the same two representative cases as in §3.1: ($y_0 = 0.15/\alpha$, $\alpha = 0.11$) and ($y_0 = 0.35/\alpha$, $\alpha = 0.06$) (figure 4a,b). For $Re = 10$, in both cases the inertia is significantly smaller than the viscous stress throughout the channel. At larger values of Re , $I(r)$ eventually exceeds $V(r)$, but the cross-over radius r_* is larger than that predicted from the stresslet coefficients (table 2).

We can rationalize the larger values of the cross-over radius αr_* by considering the boundary conditions on the channel walls. Because the velocity field \mathbf{u} vanishes on the channel walls, the inertial stresses vanish there. Therefore $I(r)$ is suppressed at larger radii. We see less suppression of $V(r)$, presumably because viscous stresses do not need to vanish on the channel walls. Suppression of $I(r)$ increases the cross-over radius at which inertial stresses must be considered in the dominant balance.

4. A series expansion for the inertial lift force

Our careful evaluation of the stresslet prefactors and wall contributions shows that viscous stresses are dominant over inertial stresses over much of the fluid-filled

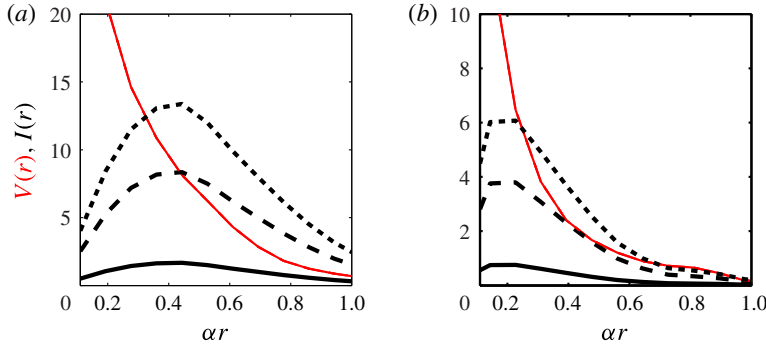


FIGURE 4. (Colour online) The dominant balance that arises from the stresslet and first wall correction of the flow for (a) a particle near the channel centre ($y_0 = 0.15/\alpha$ and $\alpha = 0.11$) and (b) a particle near the channel walls ($y_0 = 0.35/\alpha$ and $\alpha = 0.06$). The viscous stresses $V(r)$ for various Reynolds numbers are plotted as thin (red) lines, and the inertial stresses $I(r)$ are plotted as thick (black) lines. Reynolds numbers are indicated by line style: $Re = 10$, solid line; $Re = 50$, dashed line; and $Re = 80$, dotted line.

domain, including at much greater distances from the particle than previous estimates have suggested. We therefore develop an asymptotic theory, based on Cox & Brenner (1968) and Ho & Leal (1974), in which the flow field \mathbf{u} , pressure p , particle velocity \mathbf{U}_p and rotation $\boldsymbol{\Omega}_p$ are expanded in powers of Re_p , with inertia completely neglected in the leading-order equations:

$$\mathbf{u} = \mathbf{u}^{(0)} + Re_p \mathbf{u}^{(1)} + \dots, \quad p = p^{(0)} + Re_p p^{(1)} + \dots, \quad \text{etc.} \tag{4.1a,b}$$

Notice that this is an expansion in the particle Reynolds number Re_p and not the channel Reynolds number Re . Although in experiments the channel Reynolds number is typically large, the expansion is formally valid provided that α^2 is small enough that $Re_p = \alpha^2 Re \lesssim 1$. In fact, when we compare our theory with numerical simulations in § 4.5, we find that the perturbative series gives a good approximation to the lift force even for $Re_p = 7$ (figure 1b).

First we compute the first two terms in the perturbative series $\mathbf{u}^{(0)} + Re_p \mathbf{u}^{(1)}$ numerically, showing that retaining these two terms gives the lift force quantitatively accurately over the entire dynamical range of experiments.

Series-expanding (2.4) and collecting like terms in Re_p we arrive at equations for $(\mathbf{u}^{(0)}, p^{(0)})$, the first-order velocity and pressure:

$$\nabla^2 \mathbf{u}^{(0)} - \nabla p^{(0)} = \mathbf{0}, \quad \nabla \cdot \mathbf{u}^{(0)} = 0, \tag{4.2a}$$

$$\mathbf{u}^{(0)} = \mathbf{U}_p^{(0)} + \boldsymbol{\Omega}_p^{(0)} \times \mathbf{r} - \bar{\mathbf{u}} \quad \text{on } r = 1, \tag{4.2b}$$

$$\mathbf{u}^{(0)} = \mathbf{0} \quad \text{on channel walls and as } z \rightarrow \pm\infty. \tag{4.2c}$$

Similarly, the next-order velocity and pressure $(\mathbf{u}^{(1)}, p^{(1)})$ satisfy the equations:

$$\nabla^2 \mathbf{u}^{(1)} - \nabla p^{(1)} = (\bar{\mathbf{u}} \cdot \nabla \mathbf{u}^{(0)} + \mathbf{u}^{(0)} \cdot \nabla \bar{\mathbf{u}} + \mathbf{u}^{(0)} \cdot \nabla \mathbf{u}^{(0)}), \quad \nabla \cdot \mathbf{u}^{(1)} = 0, \tag{4.3a}$$

$$\mathbf{u}^{(1)} = \mathbf{U}_p^{(1)} + \boldsymbol{\Omega}_p^{(1)} \times \mathbf{r} \quad \text{on } r = 1, \tag{4.3b}$$

$$\mathbf{u}^{(1)} = \mathbf{0} \quad \text{on channel walls and as } z \rightarrow \pm\infty. \tag{4.3c}$$

For both cases, we only need to solve the Stokes equations with a known body force term. In (4.2), the body force term is equal to $\mathbf{0}$; in (4.3) the body force term is equal to the inertia of flow $\mathbf{u}^{(0)}$.

In fact, we can apply Lorentz’s reciprocal theorem (Leal 1980) to calculate the lift force associated with $\mathbf{u}^{(1)}$ without needing to directly solve (4.3). We define the test fluid flow $(\hat{\mathbf{u}}, \hat{p})$ representing Stokes flow around a sphere moving with unit velocity in the y -direction: *viz.* satisfying (4.2) with the velocity condition on the sphere replaced by $\hat{\mathbf{u}} = \mathbf{e}_y$. If $\boldsymbol{\sigma}^{(1)}$ and $\hat{\boldsymbol{\sigma}}$ are the viscous stress tensors associated with the flow fields $(\mathbf{u}^{(1)}, p^{(1)})$ and $(\hat{\mathbf{u}}, \hat{p})$ respectively, $\boldsymbol{\sigma}^{(1)} = \nabla \mathbf{u}^{(1)} + (\nabla \mathbf{u}^{(1)})^T - p^{(1)} \mathbf{1}$, etc., and $\hat{\mathbf{e}}$ and $\mathbf{e}^{(1)}$ the respective rate-of-strain tensors, $\mathbf{e}^{(1)} = [\nabla \mathbf{u}^{(1)} + (\nabla \mathbf{u}^{(1)})^T]/2$, etc., then by the divergence theorem, the following relation is valid for any volume V enclosed by a surface S :

$$\int_S (\mathbf{n} \cdot \hat{\boldsymbol{\sigma}} \cdot \mathbf{u}^{(1)} - \mathbf{n} \cdot \boldsymbol{\sigma}^{(1)} \cdot \hat{\mathbf{u}}) \, ds = \int_V [\nabla \cdot (\hat{\boldsymbol{\sigma}} \cdot \mathbf{u}^{(1)}) - \nabla \cdot (\boldsymbol{\sigma}^{(1)} \cdot \hat{\mathbf{u}})] \, dv. \tag{4.4}$$

By setting V equal to the fluid-filled domain and substituting boundary conditions from (2.4), we deduce that

$$\begin{aligned} U_p^{(1)} \cdot \int_S (\hat{\boldsymbol{\sigma}} \cdot \mathbf{n}) \, ds + \int_S (\boldsymbol{\Omega}_p^{(1)} \times \mathbf{r}) \cdot \hat{\boldsymbol{\sigma}} \cdot \mathbf{n} \, ds - \mathbf{e}_y \cdot \int_S \boldsymbol{\sigma}^{(1)} \cdot \mathbf{n} \, ds \\ = \int_V [(\nabla \cdot \boldsymbol{\sigma}^{(1)}) \cdot \hat{\mathbf{u}} + \boldsymbol{\sigma}^{(1)} : \hat{\mathbf{e}} - (\nabla \cdot \hat{\boldsymbol{\sigma}}) \cdot \mathbf{u}^{(1)} - \hat{\boldsymbol{\sigma}} : \mathbf{e}^{(1)}] \, dv. \end{aligned} \tag{4.5}$$

On the left-hand side of the equation, the first term is zero by symmetry. Similarly, the integrand of the second term can be rearranged to

$$(\boldsymbol{\Omega}_p^{(1)} \times \mathbf{r}) \cdot \hat{\boldsymbol{\sigma}} \cdot \mathbf{n} = \boldsymbol{\Omega}_p^{(1)} \cdot (\mathbf{r} \times \hat{\boldsymbol{\sigma}} \cdot \mathbf{n}), \tag{4.6}$$

which also integrates to zero. On the right-hand side of (4.5), the third term is zero by definition (since $\hat{\mathbf{u}}$ solves the Stokes equations). Furthermore, we can rearrange the second and fourth terms to

$$\boldsymbol{\sigma}^{(1)} : \hat{\mathbf{e}} - \hat{\boldsymbol{\sigma}} : \mathbf{e}^{(1)} = 2\mathbf{e}^{(1)} : \hat{\mathbf{e}} - p^{(1)} \nabla \cdot \hat{\mathbf{u}} - 2\hat{\mathbf{e}} : \mathbf{e}^{(1)} + \hat{p} \nabla \cdot \mathbf{u}^{(1)} = 0, \tag{4.7}$$

since both flows are incompressible. So, on the right-hand side of (4.5), only the first term of the volume integral remains. Using the definitions of $\boldsymbol{\sigma}^{(1)}$ and $\hat{\boldsymbol{\sigma}}$, we obtain the following formula, which we refer to as the reciprocal theorem:

$$\mathbf{e}_y \cdot \mathbf{F}_L = \int_V \hat{\mathbf{u}} \cdot (\bar{\mathbf{u}} \cdot \nabla \mathbf{u}^{(0)} + \mathbf{u}^{(0)} \cdot \nabla \bar{\mathbf{u}} + \mathbf{u}^{(0)} \cdot \nabla \mathbf{u}^{(0)}) \, dv. \tag{4.8}$$

We have now reduced our calculation of the lift force to that of solving two homogeneous Stokes equations and performing a volume integral. Numerically, we let V be the truncated numerical domain modelled by our FEM. Next we solve numerically for $\mathbf{u}^{(0)}$ from (4.2) and $\hat{\mathbf{u}}$. Again, we choose $U_p^{(0)}$ and $\boldsymbol{\Omega}_p^{(0)}$ so that the particle travels force-free and torque-free. We compute the lift force using the reciprocal theorem in (4.8) for particles at two different channel positions (figure 5a,b). We see close quantitative agreement between the lift force computed from the full NSEs and the lift force computed from the reciprocal theorem using the two-term expansion in Re_p . The comparison is accurate even when, as for $y_0 = 0.15/\alpha$, there is no simple scaling law for the dependence of F_L upon a (figure 5a). In the next section, we develop a model that nevertheless allows analytic evaluation of the lift force.

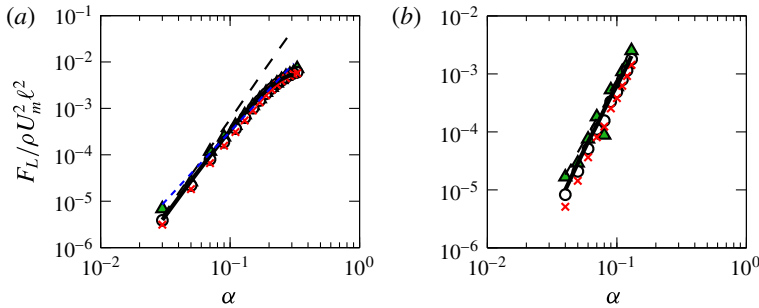


FIGURE 5. (Colour online) Numerical computation of the scaled lift force $F_L/\rho U_m^2 \ell^2$ using the NSEs in (2.4) as a function of particle size α for various channel Reynolds numbers: $Re = 10$ (triangles), $Re = 50$ (circles) and $Re = 80$ (crosses). The dashed (black) line represents a scaling law with exponent 4, i.e. $F_L \sim \rho U_m^2 \alpha^2 a^2$ as in Ho & Leal (1974), while the dotted (blue) line represents a scaling law with exponent 3, i.e. $F_L \sim \rho U_m^2 \alpha a^2$, which is the line of best fit computed in Di Carlo *et al.* (2009). The solid line represents the regular perturbation expansion computed numerically using the reciprocal theorem in (4.8). We compare all of these force predictions at two locations in the channel: (a) a particle near the channel centre ($y_0 = 0.15/\alpha$ and $\alpha = 0.11$); and (b) a particle near the channel walls ($y_0 = 0.35/\alpha$ and $\alpha = 0.06$).

4.1. Approximation of $\mathbf{u}^{(0)}$ and $\hat{\mathbf{u}}$ by method of images

In the previous section we showed that a single regular perturbation in Re_p of Stokes equations agrees excellently with the numerically computed lift force. We calculated the terms in this perturbation series numerically; but to rationally design inertial microfluidic devices, we need an asymptotic theory for how the lift force and the inertial focusing points depend on the size of the particle and its position within the channel. We derive this theory from asymptotic expansion of $\mathbf{u}^{(0)}$ and $\hat{\mathbf{u}}$ in powers of α , the dimensionless particle size. We follow Ho & Leal (1974) and use the method of reflections to generate expansions in powers of α for the Stokes flow fields appearing in (4.8) (Happel & Brenner 1982),

$$\mathbf{u}^{(0)} = \mathbf{u}_1^{(0)} + \mathbf{u}_2^{(0)} + \mathbf{u}_3^{(0)} + \mathbf{u}_4^{(0)} + \dots, \tag{4.9}$$

with similar expansions for p , $\hat{\mathbf{u}}$ and \hat{p} . Here, $\mathbf{u}_1^{(0)}$ is the Stokes solution for a particle in unbounded flow, $\mathbf{u}_2^{(0)}$ is the Stokes solution with boundary condition $\mathbf{u}_2^{(0)} = -\mathbf{u}_1^{(0)}$ on the channel walls, and $\mathbf{u}_3^{(0)}$ is the Stokes solution with boundary condition $\mathbf{u}_3^{(0)} = -\mathbf{u}_2^{(0)}$ on the particle surface, etc. Odd terms impose the global boundary conditions on the particle, whereas even terms impose the global boundary conditions on the channel walls. We will show below that the terms in this series constitute a power series in α .

Since the odd terms in the expansion, $\mathbf{u}_{2i-1}^{(0)}$, are prescribed on the sphere’s surface, they can be calculated using Lamb’s method for solving the flow external to a sphere (Lamb 1945; Happel & Brenner 1982). This method expands the velocity field as a sum of multipoles located at the sphere centre, namely,

$$\mathbf{u}_{2i-1}^{(0)} = \sum_{n=0}^{\infty} \frac{1}{r^{n+1}} \mathbf{f}_n^i \left(\frac{x-x_0}{r}, \frac{y-y_0}{r}, \frac{z}{r} \right), \tag{4.10}$$

where each term f_n^i/r^{n+1} is a combination of the stokeslet n -pole and the source $(n - 1)$ -pole. We can similarly expand the odd terms of $\hat{\mathbf{u}}$ as:

$$\hat{\mathbf{u}}_{2i-1} = \sum_{n=0}^{\infty} \frac{1}{r^{n+1}} \mathbf{g}_n^i \left(\frac{x-x_0}{r}, \frac{y-y_0}{r}, \frac{z}{r} \right). \tag{4.11}$$

The full analytic forms for the f_n^1 and g_n^1 are listed in appendix C. From the analytic form of $\mathbf{u}_1^{(0)}$, we can find $\mathbf{u}_2^{(0)}$ by solving the associated Stokes problem numerically. Given $-\mathbf{u}_2^{(0)}$ on the particle surface, we can appeal to Lamb’s solution to find $\mathbf{u}_3^{(0)}$, and so on. The same sequence of reflections can be used to expand the reference velocity $\hat{\mathbf{u}}$.

4.2. *Approximation to the reciprocal theorem integral*

Given the Stokes velocities $\mathbf{u}^{(0)}$ and $\hat{\mathbf{u}}$, we can compute the inertial lift force F_L up to terms of $O(Re_p)$ using the reciprocal theorem (4.8). As in Ho & Leal (1974), it is advantageous to divide the fluid-filled domain V into two subdomains, V_1 and V_2 , where

$$V_1 = \{r \in V : r \leq \xi\} \quad \text{and} \quad V_2 = \{r \in V : r \geq \xi\}. \tag{4.12a,b}$$

The intermediate radius ξ is any parameter satisfying $1 \ll \xi \ll 1/\alpha$. Call the corresponding integrals the inner integral and the outer integral, and identify their contributions to the lift force as F_{L_1} and F_{L_2} , respectively ($F_L = F_{L_1} + F_{L_2}$). The division of the integral into inner and outer regions allows one to incorporate varying length scales (α for the inner region and ℓ for the outer region) into our model. Note that, distinct from Schonberg & Hinch (1989), inertia remains subdominant even in the outer region V_2 . In the next two sections, we will separately consider the contributions from the inner and outer integrals.

4.3. *The inner integral*

For the inner integral, we continue to scale lengths by a , so that $1 \leq r \leq \xi \ll \alpha^{-1}$. The inner integral can be expressed as the following expansion in α :

$$F_{L_1} = \rho U_m^2 a^2 (h_4 \alpha^2 + h_5 \alpha^3 + \dots). \tag{4.13}$$

In order to calculate the terms h_4 and h_5 , we sort the terms of the Stokes velocities by leading order in α . The terms contributing at $O(\alpha^2)$ in the inner region are

$$\mathbf{u}_1^{(0)} \sim \alpha \left(\frac{1}{r^2} \mathbf{f}_1^1 + \frac{1}{r^4} \mathbf{f}_3^1 \right), \quad \hat{\mathbf{u}}_1 \sim \frac{1}{r} \mathbf{g}_0^1 + \frac{1}{r^3} \mathbf{g}_2^1, \quad \bar{\mathbf{u}} \sim \gamma \alpha r. \tag{4.14a-c}$$

All of these terms are known analytically (see appendix C), and it can be shown that their contribution to the inner integral evaluates to zero, i.e. $h_4 = 0$.

At $O(\alpha^3)$ the velocity terms contributing to calculation of h_5 are

$$\left. \begin{aligned} \mathbf{u}_1^{(0)} &\sim \alpha \left(\frac{1}{r^2} \mathbf{f}_1^1 + \frac{1}{r^4} \mathbf{f}_3^1 \right) + \alpha^2 \left(\frac{1}{r^3} \mathbf{f}_2^1 + \frac{1}{r^5} \mathbf{f}_4^1 \right), & \bar{\mathbf{u}} &\sim \gamma \alpha r + \delta \alpha^2 r^2, \\ \hat{\mathbf{u}}_1 &\sim \frac{1}{r} \mathbf{g}_0^1 + \frac{1}{r^3} \mathbf{g}_2^1, & \hat{\mathbf{u}}_2 &\sim \alpha \mathcal{S} \left[\frac{1}{r} \mathbf{g}_0^1 \right]_0, & \hat{\mathbf{u}}_3 &\sim \alpha \left(\frac{1}{r} \mathbf{g}_3^1 + \frac{1}{r^3} \mathbf{g}_2^1 \right), \end{aligned} \right\} \tag{4.15}$$

where we define $\mathbf{v} \equiv \mathcal{S}[\mathbf{u}]$ as the image of the function \mathbf{u} , and we define $\mathbf{v}_0 \equiv \mathcal{S}[\mathbf{u}]_0$ as the velocity \mathbf{v} evaluated at the particle centre. That is, \mathbf{v} solves the Stokes equations with boundary condition $\mathbf{v} = -\mathbf{u}$ on the channel walls, and $\mathbf{v}_0 = \mathbf{v}(x_0, y_0, 0)$. We determine $\mathcal{S}[(1/r)\mathbf{g}_0^1]$ numerically, by discretizing Stokes equations as an FEM, with quadratic elements for the velocity field and linear elements for the pressure field, and solving the FEM in Comsol Multiphysics.

The $O(\alpha^3)$ contribution to the inner integral is

$$\begin{aligned} h_5 &= \int_{\mathbb{R}^3} (\hat{\mathbf{u}}_1 + \hat{\mathbf{u}}_2 + \hat{\mathbf{u}}_3) \cdot (\bar{\mathbf{u}} \cdot \nabla \mathbf{u}_1^{(0)} + \mathbf{u}_1^{(0)} \cdot \nabla \bar{\mathbf{u}} + \mathbf{u}_1^{(0)} \cdot \nabla \mathbf{u}_1^{(0)}) \, d\mathbf{v} \\ &= \int_{\mathbb{R}^3} \hat{\mathbf{u}}_1 \cdot (\bar{\mathbf{u}} \cdot \nabla \mathbf{u}_1^{(0)} + \mathbf{u}_1^{(0)} \cdot \nabla \bar{\mathbf{u}} + \mathbf{u}_1^{(0)} \cdot \nabla \mathbf{u}_1^{(0)}) \, d\mathbf{v} \end{aligned} \tag{4.16}$$

where we have made use of the fact that the contributions to the integral from $\hat{\mathbf{u}}_2$ and $\hat{\mathbf{u}}_3$ evaluate to zero. Since all of the terms in the integrand are $O(r^3)$ as $r \rightarrow \infty$, we can take $\xi \rightarrow \infty$; *viz.*, replace integration over V_1 by integration over \mathbb{R}^3 . In doing so, we pick up an error that is $O(1/\xi)$. We neglect this contribution, since $\xi \gg 1$; in fact the error terms can be shown to cancel with corresponding contributions from the outer integral if expansions are continued to higher-order powers of α . Evaluating the final integral, we obtain

$$F_{L_1} = \frac{\rho U_m^2 h_5 a^5}{\ell^3} + O(a^6), \tag{4.17}$$

where

$$h_5 = -\frac{26\,171\pi\gamma_y^2}{277\,200} - \frac{53\pi\gamma_y\delta_{xx}}{1728} - \frac{283\pi\gamma_y\delta_{yy}}{3150} \tag{4.18}$$

is $O(1)$, and depends only on the location of the particle. Recall that the constants γ_y , δ_{xx} and δ_{yy} were defined in the expansion of $\bar{\mathbf{u}}$ in (2.2), and depend on the particle position.

4.4. The outer integral

For the outer integral, we will consider alternative dimensionless variables, by using the rescaled distance $\mathbf{R} = \alpha\mathbf{r}$. This corresponds to using ℓ to non-dimensionalize lengths, rather than a . We call these variables the outer variables, and we will denote them with upper-case roman letters. A detailed comparison of the dimensionless variables is given in appendix A.

In the outer region V_2 , we must express our functions in terms of \mathbf{R} and rearrange our functions by order of magnitude in α . These expansions are listed in full in appendix D. In the outer region, the reciprocal theorem integral takes the dimensional form

$$F_{L_2} = \rho U_m^2 \ell^2 \int_{V_C} \hat{\mathbf{U}} \cdot (\bar{\mathbf{U}} \cdot \nabla \mathbf{U}^{(0)} + \mathbf{U}^{(0)} \cdot \nabla \bar{\mathbf{U}} + \mathbf{U}^{(0)} \cdot \nabla \mathbf{U}^{(0)}) \, d\mathbf{v}, \tag{4.19}$$

where we have expanded our domain of integration from $V_2 = \{\mathbf{R} \in V : R \geq \xi\}$ to the entire empty channel V_C . This expansion of the domain is justified since the contribution from the region that we add to the integral $\{\mathbf{R} : 0 \leq R \leq \alpha\xi\}$ is $O(\alpha^4\xi)$, and $\xi \ll 1/\alpha$. In fact, this residue (which would show up in the $O(\alpha^3)$ inner integral) is exactly zero.

As we did for the inner integral, we can write the outer integral as an expansion in α :

$$F_{L_2} = \rho U_m^2 \ell^2 (k_4 \alpha^4 + k_5 \alpha^5 + \dots). \tag{4.20}$$

The velocity terms that contribute to k_4 are the following:

$$\left. \begin{aligned} \mathbf{U}_1^{(0)} &\sim \alpha^3 \frac{1}{R^2} \mathbf{f}_1^1, & \mathbf{U}_2^{(0)} &\sim \alpha^3 \mathcal{S} \left[\frac{1}{R^2} \mathbf{f}_1^1 \right], \\ \hat{\mathbf{U}}_1 &\sim \alpha \frac{1}{R} \mathbf{g}_0^1, & \hat{\mathbf{U}}_2 &\sim \alpha \mathcal{S} \left[\frac{1}{R} \mathbf{g}_0^1 \right], & \bar{\mathbf{U}} &\sim \gamma R + \delta R^2 + \dots \end{aligned} \right\} \quad (4.21)$$

Again, we define $\mathbf{V} = \mathcal{S}[\mathbf{U}]$ as the image of the function \mathbf{U} , and we compute $\mathcal{S}[(1/R^2)\mathbf{f}_1^1]$ and $\mathcal{S}[(1/R)\mathbf{g}_0^1]$ numerically. Furthermore, we can approximate the term \mathbf{f}_1^1 by the stresslet terms, since the rotlet terms have coefficients that are order $O(\alpha^2)$ higher than the coefficients of the stresslet terms. The $O(\alpha^4)$ contribution to the reciprocal theorem integral takes the following form:

$$k_4 = \int_{V_c} (\hat{\mathbf{U}}_1 + \hat{\mathbf{U}}_2) \cdot [\bar{\mathbf{U}} \cdot \nabla(\mathbf{U}_1^{(0)} + \mathbf{U}_2^{(0)}) + (\mathbf{U}_1^{(0)} + \mathbf{U}_2^{(0)}) \cdot \nabla \bar{\mathbf{U}}] dv. \quad (4.22)$$

We run into a problem numerically evaluating the integral in (4.22) when considering only the first terms in the series expansions, $\mathbf{U}_1^{(0)}$ and $\hat{\mathbf{U}}_1$. The problem arises because $\mathbf{U}_1^{(0)}$ and $\hat{\mathbf{U}}_1$ have singularities of the form

$$\mathbf{U}_1^{(0)} \approx -\frac{5\gamma_y}{2} \frac{(Y - Y_0)\mathbf{Z}\mathbf{R}}{R^5}, \quad \hat{\mathbf{U}}_1 \approx \frac{3}{4} \left(\mathbf{e}_y + \frac{(Y - Y_0)\mathbf{R}}{R^2} \right) \frac{1}{R}, \quad (4.23a,b)$$

which are respectively the stresslet and stokeslet components of the two velocity fields. When the singularities are integrated against the shear term of $\bar{\mathbf{U}}$, that is $\bar{\mathbf{U}}_\gamma \approx \gamma_y Y \mathbf{e}_z$, the result is an integral that is undefined near $R = 0$:

$$\int_{R < \epsilon} \hat{\mathbf{U}}_1 \cdot [\bar{\mathbf{U}}_\gamma \cdot \nabla \mathbf{U}_1^{(0)} + \mathbf{U}_1^{(0)} \cdot \nabla \bar{\mathbf{U}}_\gamma] dv. \quad (4.24)$$

However, converting to spherical coordinates, we find that the angular dependence forces the integral in (4.24) to be zero:

$$\int_0^\pi \int_0^{2\pi} \int_0^\epsilon \left(\frac{15\gamma_y^2 (1 + 2 \cos 2\theta) \sin^4 \theta \sin^3 \phi}{4R} \right) dR d\phi d\theta = 0. \quad (4.25)$$

This angular behaviour is difficult to capture numerically, especially if the mesh is not symmetric. Instead, we propose a regularization of the outer integral, where we integrate the problematic terms analytically in a small region near $R = 0$. Now considering the full expansion of $\bar{\mathbf{u}}$, we derive the following analytic form for the integral in the region near the origin:

$$\int_{R < \epsilon} \hat{\mathbf{U}}_1 \cdot [\bar{\mathbf{U}} \cdot \nabla \mathbf{U}_1^{(0)} + \mathbf{U}_1^{(0)} \cdot \nabla \bar{\mathbf{U}}] dv = -\pi \gamma_y (\delta_{xx} + 3\delta_{yy}) \epsilon. \quad (4.26)$$

Recall that the constants γ_y , δ_{xx} and δ_{yy} were defined in the expansion of $\bar{\mathbf{u}}$ in (2.2). Using this analytic expression, we split up the rest of the reciprocal theorem integral (4.22) into the following parts:

$$\begin{aligned}
 k_4 &= \int_{V_C} \hat{U}_2 \cdot [\bar{U} \cdot \nabla(U_1^{(0)} + U_2^{(0)}) + (U_1^{(0)} + U_2^{(0)}) \cdot \nabla \bar{U}] \, dv \\
 &+ \int_{V_C} \hat{U}_1 \cdot [\bar{U} \cdot \nabla U_2^{(0)} + U_2^{(0)} \cdot \nabla \bar{U}] \, dv \\
 &+ \int_{\{r \in V_C : R \geq \epsilon\}} \hat{U}_1 \cdot [\bar{U} \cdot \nabla U_1^{(0)} + U_1^{(0)} \cdot \nabla \bar{U}] \, dv \\
 &- \pi \gamma_y (\delta_{xx} + 3\delta_{yy}) \epsilon.
 \end{aligned} \tag{4.27}$$

The first three lines in (4.27) are evaluated numerically using the FEM. Evaluating the integral in (4.27), we arrive at the scaling law

$$F_{L_2} = \frac{\rho U_m^2 k_4 a^4}{\ell^2} + O(\alpha^5), \tag{4.28}$$

where $k_4 = O(1)$ is a constant that depends on the location of the particle in the channel, and is computed numerically.

Similarly, the $O(\alpha^5)$ correction to the outer integral comes from terms

$$\left. \begin{aligned}
 U_1^{(0)} &\sim \alpha^3 \frac{1}{R^2} f_1^1, & U_2^{(0)} &\sim \alpha^3 \mathcal{S} \left[\frac{1}{R^2} f_1^1 \right], \\
 \hat{U}_3 &\sim \alpha^2 \frac{1}{R} g_0^3, & \hat{U}_4 &\sim \alpha^2 \mathcal{S} \left[\frac{1}{R} g_0^3 \right], & \bar{U} &\sim \gamma R + \delta R^2 + \dots
 \end{aligned} \right\} \tag{4.29}$$

Again, we must regularize the outer integral, since \hat{U}_3 also has a Stokeslet singularity. We use the same regularization as before, replacing \hat{U}_1 and \hat{U}_2 with \hat{U}_3 and \hat{U}_4 , respectively.

Finally, combining terms at $O(\alpha^4)$ and $O(\alpha^5)$, we obtain

$$f_{L_2} = \frac{\rho U_m^2 k_4 a^4}{\ell^2} + \frac{\rho U_m^2 k_5 a^5}{\ell^3} + O(\alpha^6), \tag{4.30}$$

where $k_5 = O(1)$ is a constant that depends on the location of the particle in the channel. We have now calculated the V_2 contribution to the reciprocal theorem integral up to order $O(\alpha^5)$.

4.5. Results

In the last section, we described our method of computing the correction to the scaling law made by Ho & Leal (1974). Combining the inner and outer integrals, the result is a new approximation of the form

$$F_L = \frac{\rho U_m^2 c_4 a^4}{\ell^2} + \frac{\rho U_m^2 c_5 a^5}{\ell^3} + O(\alpha^6), \tag{4.31}$$

where $c_4 = k_4$ from (4.27), and $c_5 = h_5 + k_5$ from (4.18) and (4.30). The prefactors c_4 and c_5 are $O(1)$ in α , and depend only on the location of the particle in the channel. The extended series agrees well with numerical data for particle sizes up to $\alpha = 0.2\text{--}0.3$ (figure 6). This calculation could in principle be extended by

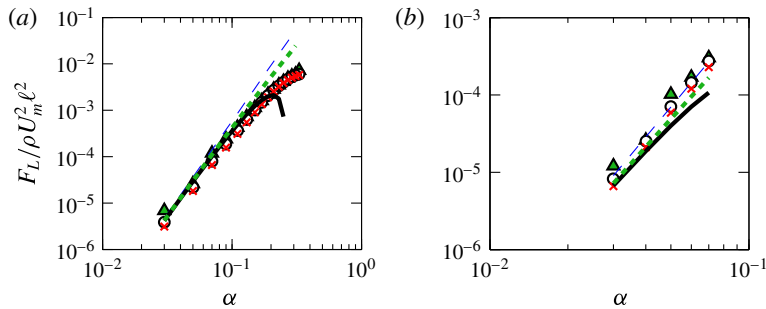


FIGURE 6. (Colour online) Numerical computation of the lift force F_L using the NSEs in (2.4) and plotted as a function of particle radius a for channel Reynolds numbers $Re = 10$ (triangles), $Re = 50$ (circles) and $Re = 80$ (crosses). The dashed (blue) line represents a scaling law of particle radius to the fourth power, $F_L = \rho U_m^2 c_4 \alpha^2 a^2$, the solid (black) line represents the sum of the fourth and fifth power terms in (4.31), and the dotted (green) line represents the completion of series in (4.32), with (a) particle displacement $y_0 = 0.15/\alpha$ and (b) particle displacement $y_0 = 0.4/\alpha$.

computing the contributions from higher-order terms. Completing the series (Hinch 1991), i.e. approximating

$$F_L \approx \frac{\rho U_m^2 c_4 a^4}{\ell^2 \left(1 - \frac{c_5 a}{c_4 \ell}\right)}, \quad (4.32)$$

produces a modest increase in the accuracy of the asymptotic approximation (figure 6).

By including two terms in our asymptotic expansion, we can describe how the particle equilibrium position depends on its size – a key prediction for rationally designing devices that use inertial lift forces to fractionate particles, or to transfer them between fluid streams (Di Carlo *et al.* 2009; Hur *et al.* 2010; Mach *et al.* 2011; Chung *et al.* 2013; Sollier *et al.* 2014) (figure 8). We compare our asymptotic calculation predictions directly with experiments of Di Carlo *et al.* (2009), finding good agreement in focusing positions up to $a = 0.3$ (figure 8b).

5. Three-dimensional asymptotic expansion

Previous asymptotic studies have considered inertial migration in 2D flows (Ho & Leal 1974; Schonberg & Hinch 1989; Hogg 1994; Asmolov 1999). At sufficiently small values of a , there is qualitative agreement between the 2D theories and our theory, but only when the particle is located on a symmetry plane, e.g. $x_0 = 0$ or $y_0 = 0$. However, real inertial microfluidic devices focus in x - and y -directions, taking initially uniformly dispersed particles to four focusing positions. Our asymptotic approach allows us to compute the focusing forces for particles placed at arbitrary positions in the channel.

The calculation is very similar to the one outlined in §4; we only need to add similar terms driven by the shear in the x -direction, and allow for a reciprocal velocity \hat{u} associated with moving the particle in this direction. The full Lamb's solution for $\mathbf{u}_1^{(0)}$ has additional terms from the shear in the x -direction (i.e. the terms with coefficients γ_x), shown in appendix C. The only additional components of $\mathbf{u}_1^{(0)}$ that contribute to the 3D calculation are the stresslet and source quadrupole.

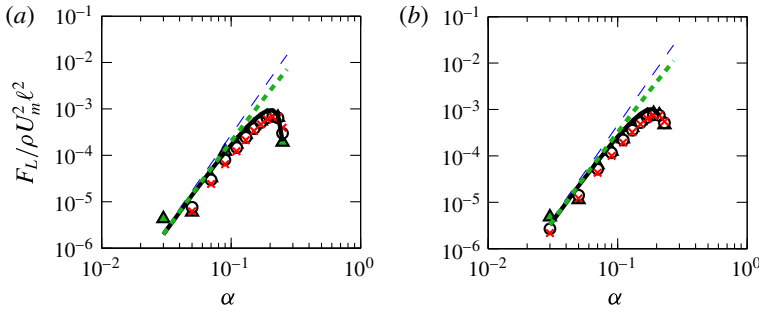


FIGURE 7. (Colour online) Numerical computation of the lift force F_L from (2.4) as a function of particle radius for channel Reynolds numbers $Re = 10$ (triangles), $Re = 50$ (circles) and $Re = 80$ (crosses). The dashed (blue) line represents a scaling law of particle radius to the fourth power, $F_L = \rho U_m^2 c_4 \alpha^2 a^2$, the solid (black) line represents the fifth power correction term in (5.4), and the dotted (green) line represents the completion of series in (4.32), with particle displacement $x_0 = 0.2/\alpha$ and $y_0 = 0.15/\alpha$ for lift force (a) in the x -direction and (b) in the y -direction.

The inner integral in 3D evaluates to

$$F_{L_1}^{(3D)} = \frac{\rho U_m^2 h_5^{(3D)} a^5}{\ell^3} + O(a^6), \tag{5.1}$$

where

$$h_5^{(3D)} = \frac{4381\pi\gamma_x\gamma_y}{554\,400} - \frac{26\,171\pi\gamma_y^2}{277\,200} + \frac{527\pi\psi_y\gamma_x\gamma_y}{116\,424} - \frac{53\pi\gamma_y\delta_{xx}}{1728} + \frac{19\pi\gamma_x\delta_{yy}}{3150} - \frac{283\pi\gamma_y\delta_{yy}}{3150}. \tag{5.2}$$

We define ψ_y to be the value of the y -component of the image of the stokeslet evaluated at the location of the particle:

$$\psi_y = \left[\mathcal{S} \left[\frac{1}{r} \mathbf{g}_0^1 \right] \cdot \mathbf{e}_y \right] \Big|_{(x,y,z)=(x_0,y_0,0)}, \tag{5.3}$$

where \mathbf{g}_0^1 is the stokeslet and the leading term of $\hat{\mathbf{u}}_1$ defined in (C 8) in appendix C. The outer integral remains the same; however, $\mathbf{u}_1^{(0)}$ and $\mathbf{u}_3^{(0)}$ each now include a stresslet contribution associated with shear in the x -direction. Computing this integral gives a scaling law of the form

$$F_L^{(3D)} = \frac{\rho U_m^2 c_4^{(3D)} a^4}{\ell^2} + \frac{\rho U_m^2 c_5^{(3D)} a^5}{\ell^3} + O(a^6). \tag{5.4}$$

It remains true that, for particles located arbitrarily in the square channel, the lift force scales like a^4 in the asymptotic limit $\alpha \rightarrow 0$. Additionally, our $O(a^5)$ correction to the scaling law remains accurate for moderately large α , shown in figure 7(a,b) for the forces in the x - and y -direction, respectively. We provide the calculated values of the 3D lift force in a square channel in a Matlab code in the supplementary data available at <http://dx.doi.org/10.1017/jfm.2014.739>. In particular, we find that

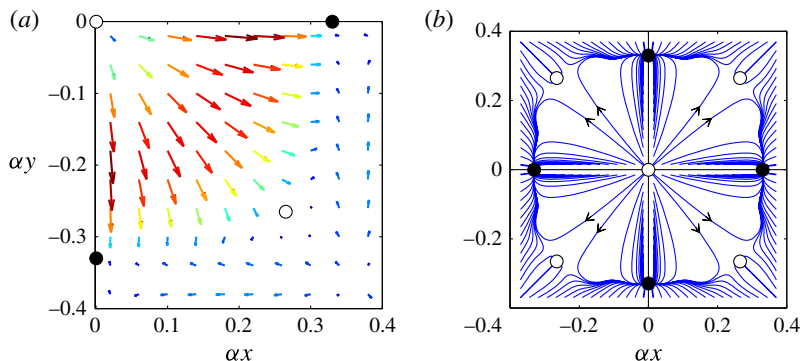


FIGURE 8. (Colour online) (a) Lift force calculated using (5.4) for locations in the lower right quadrant of the channel for a particle of radius $\alpha = 0.11$ and $Re = 80$. The solid (black) circles mark stable equilibrium points, while the open (white) circles mark unstable equilibrium points. (b) Trajectories of particles calculated using (5.5) for particle size $\alpha = 0.11$ and $Re = 80$. The solid (black) circles mark stable equilibrium points, while the open (white) circles mark unstable equilibrium points.

lift forces vanish only at eight symmetrically placed points around the channel, with four points being stable and four unstable, in good agreement with experimental observations (figure 8a).

We can compute particle streamlines using the lift force prediction, and confirm that there are four stable focusing positions in the channel (figure 8b). Particles are advected using a forward Euler time stepping scheme. We find the particle velocity by equating the $O(a^5)$ lift force (5.4) with the $O(a)$ drag force (Happel & Brenner 1982). That is, v_L , the y -component of velocity v , satisfies the equation

$$6\pi\mu a(v_L + \psi_y) = \left[\frac{\rho U_m^2 c_4^{(3D)} a^4}{\ell^2} + \frac{\rho U_m^2 c_5^{(3D)} a^5}{\ell^3} \right] \Bigg|_{(x_0, y_0, 0)}, \quad (5.5)$$

where ψ_y is the image velocity of the stokeslet defined in (5.3). The velocity u_L , the x -component of velocity u , is computed in the same way by substituting ψ_x from the x -stokeslet for ψ_y .

In addition, the distance of the focusing positions from the channel centre-line can be predicted by solving the implicit equation $F_L^{(3D)} = 0$. Recall that the lift force coefficients depend on the location of the particle, i.e. $c_4^{(3D)} = c_4^{(3D)}(x_0, y_0)$ and $c_5^{(3D)} = c_5^{(3D)}(x_0, y_0)$. Since the lift force formula has both $O(a^4)$ and $O(a^5)$ terms, the focusing position will have a functional dependence on the particle size a . This prediction of the focusing position compares well with experimental data by Di Carlo *et al.* (2009), especially for particle sizes up to $\alpha \leq 0.3$ (figure 9b).

6. Discussion

Our findings resolve confusion about the size dependence of inertial lift forces experienced by particles travelling through microchannels. Many asymptotic and numerical studies have been employed to determine how the lateral force scales with particle radius, and have found power laws with exponents 2, 3, 4 and 5. By numerically dissecting the equations of fluid flow around the particle, we find that

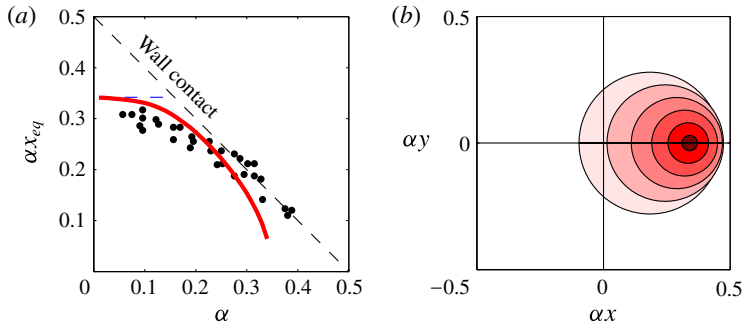


FIGURE 9. (Colour online) (a) Inertial focusing position as a function of particle size predicted by our theory. The markers are data collected by Di Carlo *et al.* (2009), the dashed (blue) line is the theory predicted by the first term of $O(\alpha^4)$ in (4.31), and the solid (red) line is the theory predicted by (4.31). (b) Schematic diagram plotting the outlines of particles at their predicted focusing position along the positive x -axis. The particle sizes range between $\alpha = 0.03$ and $\alpha = 0.29$.

viscous stresses dominate over inertial stresses even at moderate channel Reynolds numbers. We rationalize this finding by showing that this ordering of fluxes is inherited from the stresslet flow field approximation to the far field of a particle, provided that the contribution from channel walls is included. We make use of this fact to develop a perturbation series expansion for the lift force, extending the theory of Ho & Leal (1974) both to three dimensions and to include $O(\alpha^5)$ sized terms. We find that the scaling is a power law with exponent 4 for asymptotically small particle radius, but that additional terms must be included to predict lift forces for the range of particle sizes and flow speeds accessed in real inertial microfluidic devices. By including these additional terms, we are also able to predict asymptotically how focusing position depends on particle size.

Somewhat surprisingly, the regular perturbation expansion accurately predicts the particle lift force even at channel Reynolds numbers and particle sizes where the parameters in our expansion are not small (e.g. up to $Re_p \approx 10$). This is consistent with our determination that inertial stress fluxes scale simply with U^2 even outside of the regime of velocities and channel sizes at which viscous stresses are numerically larger than momentum fluxes. Thus, although assuming a viscous stress–pressure dominant balance is not justified based on simple comparison of the order of magnitude of terms, the perturbation expansion continues to give good results.

We hope that the results in this paper will provide a first step towards predictive theory for the design of inertial microfluidic devices. The biggest unmet challenge here is to determine whether unsteady effects scale like momentum fluxes for determining dominant balances. If the unsteady scaling can be established, then it will be possible to model time-varying problems, including the migration of particles in non-rectilinear geometries, such as the microcentrifuge, or the interactions of particles, such as the recently discovered phenomena of self-organization by inertially focused particles into stably ordered chains (Humphry *et al.* 2010; Lee *et al.* 2010). We have shown that the viscous–pressure stress dominant balance leads to a particularly simple far-field form to the flow disturbance, potentially allowing simplified modelling of particle interactions. Additionally we provide a Matlab code with the calculated values of the lift force in the supplementary data.

Variables	Dimensional	Inner	Outer
Distance	$\mathbf{r}' = (x', y', z')$	$\mathbf{r} = (x, y, z)$	$\mathbf{R} = (X, Y, Z)$
Velocity	\mathbf{u}'	\mathbf{u}	\mathbf{U}
Pressure	p'	p	P
Particle location	(x'_0, y'_0)	(x_0, y_0)	(X_0, Y_0)
Particle velocity	\mathbf{U}'_p	\mathbf{U}_p	\mathbf{U}_p
Particle angular velocity	$\mathbf{\Omega}'_p$	$\mathbf{\Omega}_p$	$\mathbf{\Omega}_p$
Poiseuille flow	$\bar{\mathbf{u}}'$	$\bar{\mathbf{u}}$	$\bar{\mathbf{U}}$
Asymptotic expansion of velocity	—	$\mathbf{u}^{(0)}$	$\mathbf{U}^{(0)}$
Reference velocity	—	$\hat{\mathbf{u}}$	$\hat{\mathbf{U}}$
Conversion from dimensional variables	\mathbf{r}'	$\mathbf{r} = \mathbf{r}'/a$	$\mathbf{R} = \mathbf{r}'/\ell$
Conversion from inner variables	$\mathbf{r}' = a\mathbf{r}$	\mathbf{r}	$\mathbf{R} = \alpha\mathbf{r}$
Conversion from outer variables	$\mathbf{r}' = \ell\mathbf{R}$	$\mathbf{r} = \mathbf{R}/\alpha$	\mathbf{R}

TABLE 3. Comparison of dimensional and dimensionless scalings of the variables.

Acknowledgements

This work was partly supported by the National Science Foundation through grants DGE-1144087 (to K.H.) and DMS-1312543 (to M.R.) and by a research fellowship from the Alfred P. Sloan Foundation to M.R. We thank Dino Di Carlo, Howard Stone and Z. Jane Wang for useful discussions.

Supplementary data

Supplementary data is available at <http://dx.doi.org/10.1017/jfm.2014.739>.

Appendix A. Notation

Throughout the main paper, we need to change the scaling of variables in order to capture the dynamics either near the particle or near the channel walls. In this appendix, we create a reference for the notation for three scalings: dimensional scalings, dimensionless inner variables and dimensionless outer variables. To be consistent with previous literature, we denote the dimensionless inner variables with lower-case roman letters, and the dimensionless outer variables with upper-case roman letters. We use primes to distinguish dimensional variables. A reference is presented in table 3.

We must draw attention to the notation for the particle velocity and particle angular velocity. Since both the inner and outer variables are scaled by the same velocity, αU_m , the scaled particle velocity is the same in both cases. We choose to represent the dimensionless particle velocity by \mathbf{U}_p to be consistent with notation in previous studies (Ho & Leal 1974; Schonberg & Hinch 1989).

However, the scaling for the particle angular velocity differs between the inner and outer coordinates. We continue to use $\mathbf{\Omega}_p$ in both the inner and outer variables, despite this abuse of notation. We keep $\mathbf{\Omega}_p$ in order to be consistent with previous studies (Ho & Leal 1974; Schonberg & Hinch 1989). We feel justified in our decision since $\mathbf{\Omega}_p$ does not arise in the computation of our asymptotic model, so the reader wishing to apply our results need not worry over the discrepancy. Nevertheless, we remind the reader that the particle angular velocity for the inner variables satisfies $\boldsymbol{\omega}_p = \alpha\mathbf{\Omega}_p$.

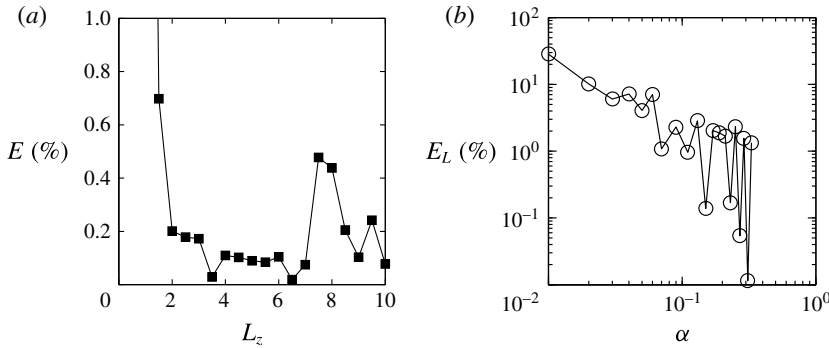


FIGURE 10. (a) The relative error E of the drag force is less than 1 % for $L_z > 1$, and in particular for our choice of $L_z = 5$ the relative error is less than 0.5 %. (b) The relative lift force error E_L from solving the NSEs increases exponentially as α decreases.

Appendix B. Accuracy of the numerical model

B.1. Accuracy of the domain size

We subjected the FEM discretization of (2.4) to convergence tests based on varying the size of the numerical domain and on changing the mesh size. Maximum element size was decreased, and the length of the domain was increased until the computed drag and lift forces had converged to within 0.5 %.

To test the length of the domain, we varied the variable L_z , defined so that the channel domain became $\ell/a \times \ell/a \times L_z(\ell/a)$. We solved the NSEs where the particle surface and channel walls have no-slip boundary conditions. The particle is assumed to have no velocity or angular velocity. Comsol’s standard meshing algorithms are used, and the particle size is chosen to be $\alpha = 0.11$.

We see that the drag force F quickly converges to its final value, at approximately $L_z = 2-3$ (figure 10a). Averaging the data for $L_z \geq 3$ to obtain a force estimate \bar{F} , we also present a relative error as $E = 100(F - \bar{F})/\bar{F}$. A small fluctuating error persists as L_z is increased up to $L_z = 10$. This error probably reflects mesh noise, rather than geometry. Similar data are seen when simulations are performed on different grades of mesh.

B.2. Accuracy of the particle size

We also discuss the range of α values that were computed in this paper. The upper range of α is limited by the position of the particle relative to the walls and to the equilibrium positions. Since the lift force F_L is a function not only of α , but also of x_0 and y_0 , for any given α , there are four coordinates (x_0, y_0) where the lift force is zero, and we call these points ‘equilibrium positions’. In the first part of our paper, we constrain our locations to those on the positive y -axis, that is, coordinates of the form $(0, y_0)$, for $y_0 > 0$. The equilibrium position $(0, y_0^*)$, which is a function of α , divides this domain into two sections: (i) the domain between the equilibrium position and the centre of the channel, and (ii) the domain between the equilibrium position and the wall. We must be careful in these regions, when we are examining the scaling law for fixed y_0 and varied α , to choose α so that f_L remains positive and does not pass through zero. The same principle extends to the choice of α for all locations throughout the channel.

The lower range of α , however, is limited by the accuracy of the root finder in the Navier–Stokes solver. As discussed in § 2, the values of U_p and Ω_p are chosen so that the particle is drag-free and force-free. Therefore, the drag force F_D can be used as a measure of the precision of the numerical solver. We define the relative lift force error as $E_L = 100(F_D/F_L)$. The relative lift force error as a function of α for a particle located at $(x_0 = 0, y_0 = 0.15/\alpha)$ and with $Re = 1$ increases exponentially as α decreases to zero (figure 10*b*). We limit $\alpha \geq 0.03$, or relative error $E_L < 10\%$.

We do not strive to test smaller particle sizes α because the theoretical results of Schonberg & Hinch (1989) and Asmolov (1999) are generally accepted to be true for asymptotically small particles. Our goal in this paper is to produce theory for particles at the sizes used in experimental systems. Smaller values of α are not used in experiments, because lift forces become too weak to compete with other forces, such as Brownian motion.

B.3. Accuracy of the Navier–Stokes solver

To further account for artifacts associated with, for example, regularization of the convective (inertial) terms in (2.4), we also solved a model problem of computing the drag force on a sphere moving through a quiescent fluid, for which a considerable body of well-validated experimental and numerical data exists (Veysey & Goldenfeld 2007).

Let a be the particle radius, Ue_z be the flow velocity, ρ the fluid density and ν be the kinematic viscosity of the fluid surrounding a particle. The Reynolds number in this scenario is $Re_p = Ua/\nu$. The drag F_D on the sphere is the force in the z -direction. We define the drag coefficient to be

$$C_D = \frac{F_D}{\rho U^2 a^2}. \quad (\text{B } 1)$$

In our simulation, we consider the domain of fluid to be a cube of length $50a$, with the particle of radius a centred at the origin. We choose the minimum element size at the sphere surface to be comparable to those of the simulations described in § 2.

We compute the drag force using the Lagrange multipliers used within the FEM to enforce the velocity boundary condition on the particle surface. We consider Reynolds numbers between $Re_p = 0.1$ and $Re_p = 100$, by varying the fluid velocity U . Our computation of the drag coefficient C_D compares favourably to those of various experimental and numerical studies (figure 11). In particular, Maxworthy (1965) accurately measures the drag on a sphere in experiments, using a container diameter that is 700 times the sphere diameter. Maxworthy estimates his experimental error to be better than 2%. We also include experimental data catalogued in Perry (1950) for larger Reynolds numbers and numerical studies by Dennis & Walker (1971) and LeClair *et al.* (1972).

Appendix C. Analytic velocities

This appendix contains the full equations for the velocities, $\mathbf{u}_1^{(0)}$ and $\hat{\mathbf{u}}_1$, described in § 4. Since the odd terms of the expansion of $\mathbf{u}^{(0)}$ are exact on the particle, they can be computed analytically using Lamb's solution for the flow external to a sphere (Lamb 1945; Ho & Leal 1974). The multipole expansion of $\mathbf{u}_1^{(0)}$ takes the form

$$\mathbf{u}_1^{(0)} = \sum_{n=0}^{\infty} \frac{1}{r^{n+1}} \mathbf{f}_n^1 \left(\frac{x-x_0}{r}, \frac{y-y_0}{r}, \frac{z}{r} \right). \quad (\text{C } 1)$$

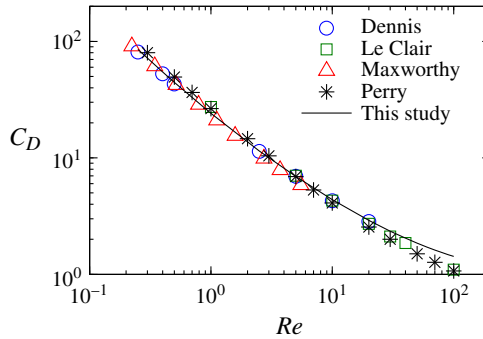


FIGURE 11. (Colour online) Our calculation of the drag coefficient, C_D , for a sphere in a uniform flow (black line) compares well to numerical data (blue circles, Dennis & Walker (1971); green squares, LeClair *et al.* (1972)) and experimental data (red triangles, Maxworthy (1965); black asterisks, Perry (1950)) across a large range of Reynolds numbers, Re .

The components of each \mathbf{f}_n^1 are defined as follows:

$$\mathbf{f}_0^1 \left(\frac{x}{r}, \frac{y}{r}, \frac{z}{r} \right) = -\frac{(A_1 + I_1)}{2} \left(\mathbf{e}_z + \frac{z\mathbf{r}}{r^2} \right), \tag{C2}$$

$$\mathbf{f}_1^1 \left(\frac{x}{r}, \frac{y}{r}, \frac{z}{r} \right) = \frac{-5\gamma_y yz\mathbf{r}}{2 r^3} + C_1 \left(\frac{z\mathbf{e}_y}{r} - \frac{y\mathbf{e}_z}{r} \right) + \frac{-5\gamma_x xz\mathbf{r}}{2 r^3} + K_1 \left(\frac{z\mathbf{e}_x}{r} - \frac{x\mathbf{e}_z}{r} \right), \tag{C3}$$

$$\begin{aligned} \mathbf{f}_2^1 \left(\frac{x}{r}, \frac{y}{r}, \frac{z}{r} \right) &= -\frac{(\delta_{yy} + \delta_{xx})}{15} \left(\mathbf{e}_z - \frac{3z\mathbf{r}}{r^2} \right) + \frac{(-\delta_{yy} + \delta_{xx})}{3} \left(\frac{z\mathbf{r}}{r^2} - \frac{(r^2 - 2y^2)\mathbf{e}_z}{r^2} \right) \\ &\quad + \frac{7\delta_{yy}}{120} \left[\left(13 - \frac{75y^2}{r^2} \right) \frac{z\mathbf{r}}{r^2} + \frac{10yz\mathbf{e}_y}{r^2} - \left(1 - \frac{5y^2}{r^2} \right) \mathbf{e}_z \right] \\ &\quad + \frac{7\delta_{xx}}{120} \left[\left(13 - \frac{75x^2}{r^2} \right) \frac{z\mathbf{r}}{r^2} + \frac{10xz\mathbf{e}_x}{r^2} - \left(1 - \frac{5x^2}{r^2} \right) \mathbf{e}_z \right], \end{aligned} \tag{C4}$$

$$\mathbf{f}_3^1 \left(\frac{x}{r}, \frac{y}{r}, \frac{z}{r} \right) = \frac{-\gamma_y}{2} \left(\frac{z\mathbf{e}_y}{r} + \frac{y\mathbf{e}_z}{r} - \frac{5yz\mathbf{r}}{r^3} \right) + \frac{-\gamma_x}{2} \left(\frac{z\mathbf{e}_x}{r} + \frac{x\mathbf{e}_z}{r} - \frac{5xz\mathbf{r}}{r^3} \right), \tag{C5}$$

$$\begin{aligned} \mathbf{f}_4^1 \left(\frac{x}{r}, \frac{y}{r}, \frac{z}{r} \right) &= \frac{\delta_{yy}}{8} \left[-5 \left(1 - \frac{7y^2}{r^2} \right) \frac{z\mathbf{r}}{r^2} + \frac{2yz\mathbf{e}_y}{r^2} + \left(1 - \frac{5y^2}{r^2} \right) \mathbf{e}_z \right] \\ &\quad + \frac{\delta_{xx}}{8} \left[-5 \left(1 - \frac{7x^2}{r^2} \right) \frac{z\mathbf{r}}{r^2} + \frac{2xz\mathbf{e}_x}{r^2} + \left(1 - \frac{5x^2}{r^2} \right) \mathbf{e}_z \right], \end{aligned} \tag{C6}$$

and $\mathbf{f}_n^1 = \mathbf{0}$ for $n \geq 5$. Here the constants A_1 , C_1 , I_1 and K_1 are all of order $O(\alpha^3)$, and so do not participate in determining the force on the particle at the order computed in this study. Note that when we are on the symmetry plane $x = 0$, then also $\gamma_x = 0$, and likewise with y and γ_y .

We can also use Lamb's solution to calculate the odd terms in the expansion of $\hat{\mathbf{u}}$. In particular, we represent $\hat{\mathbf{u}}_1$ in the following multipole expansion:

$$\hat{\mathbf{u}}_1 = \sum_{n=0}^{\infty} \frac{1}{r^{n+1}} \mathbf{g}_n^1 \left(\frac{x - x_0}{r}, \frac{y - y_0}{r}, \frac{z}{r} \right). \tag{C7}$$

The full analytic solutions for the \mathbf{g}_n^1 are below:

$$\mathbf{g}_0^1 \left(\frac{x}{r}, \frac{y}{r}, \frac{z}{r} \right) = \frac{3}{4} \left(\mathbf{e}_y + \frac{y\mathbf{r}}{r^2} \right), \tag{C8}$$

$$\mathbf{g}_2^1 \left(\frac{x}{r}, \frac{y}{r}, \frac{z}{r} \right) = \frac{1}{4} \left(\mathbf{e}_y - \frac{3y\mathbf{r}}{r^2} \right), \tag{C9}$$

and $\mathbf{g}_n^1 = \mathbf{0}$ for $n = 1$, and $n \geq 3$.

Appendix D. Determining the reciprocal theorem integrands

In this appendix, we rationalize the choice of integrands for the reciprocal theorem (4.8) in §§ 4.3 and 4.4. For each domain, we scale by the characteristic length, and then sort terms by magnitude in α . Finally, we choose terms of the velocities that combine to give the desired power of α .

D.1. Inner integral

For the inner integral, we continue to scale lengths by the particle radius a , and collect terms by order of magnitude in α . For the $O(\alpha^4)$ contribution, we need to choose combinations of $\mathbf{u}_i^{(0)}$, $\hat{\mathbf{u}}_i$ and $\bar{\mathbf{u}}$ that combine to give $O(\alpha^2)$ in the integrand of (4.8). Similarly, for $O(\alpha^3)$, terms need to combine to give $O(\alpha^3)$ in the integrand.

The leading terms in magnitude α of the $\mathbf{u}_i^{(0)}$ are

$$\mathbf{u}_1^{(0)} \sim \alpha \left(\frac{1}{r^2} \mathbf{f}_1^1 + \frac{1}{r^4} \mathbf{f}_3^1 \right) + \alpha^2 \left(\frac{1}{r^3} \mathbf{f}_2^1 + \frac{1}{r^5} \mathbf{f}_4^1 \right) + O(\alpha^4), \tag{D 1a}$$

$$\mathbf{u}_2^{(0)} \sim \alpha^3 \mathcal{S} \left[\frac{1}{r^2} \mathbf{f}_1^1 \right] + O(\alpha^4), \tag{D 1b}$$

and all higher-order $\mathbf{u}_i^{(0)}$ are $O(\alpha^4)$ or smaller. We define $\mathbf{v} = \mathcal{S}[\mathbf{u}]$ as the image of the function \mathbf{u} , that is, \mathbf{v} solves the Stokes equations with $-\mathbf{u}$ as the boundary condition on the walls. The leading terms in magnitude α of the $\hat{\mathbf{u}}_i$ are

$$\hat{\mathbf{u}}_1 \sim \frac{1}{r} \mathbf{g}_0^1 + \frac{1}{r^3} \mathbf{g}_2^1, \tag{D 2a}$$

$$\hat{\mathbf{u}}_2 \sim \alpha \mathcal{S} \left[\frac{1}{r} \mathbf{g}_0^1 \right] + O(\alpha^3), \tag{D 2b}$$

$$\hat{\mathbf{u}}_3 \sim \alpha \left(\frac{1}{r} \mathbf{g}_0^3 + \frac{1}{r^3} \mathbf{g}_2^3 \right), \tag{D 2c}$$

and higher-order $\hat{\mathbf{u}}_i$ are $O(\alpha^2)$ or smaller. The leading terms in magnitude α of $\bar{\mathbf{u}}$ are

$$\bar{\mathbf{u}} \sim [\alpha\gamma r + \alpha^2\delta r^2 + O(\alpha)]\mathbf{e}_z. \tag{D 3}$$

Recall that the inner integral has the α expansion:

$$F_{L_1} = \rho U_m^2 \alpha^2 (h_4 \alpha^2 + h_5 \alpha^5 + \dots). \tag{D 4}$$

It is evident that only $\mathbf{u}_1^{(0)}$, $\hat{\mathbf{u}}_1$ and the shear term of $\bar{\mathbf{u}}$ (call it $\bar{\mathbf{u}}_\gamma$) contribute to the $O(\alpha^4)$ term of the inner integral, that is,

$$h_4 = \int_{\mathbb{R}^3} \hat{\mathbf{u}}_1 \cdot (\bar{\mathbf{u}}_\gamma \cdot \nabla \mathbf{u}_1^{(0)} + \mathbf{u}_1^{(0)} \cdot \nabla \bar{\mathbf{u}}_\gamma) \, dv, \tag{D 5}$$

whereas $\mathbf{u}_1^{(0)}$, $\hat{\mathbf{u}}_1$, $\hat{\mathbf{u}}_2$, $\hat{\mathbf{u}}_3$ and both the shear and curvature terms of $\bar{\mathbf{u}}$ (call them $\bar{\mathbf{u}}_\gamma$ and $\bar{\mathbf{u}}_\delta$ respectively) contribute to the $O(\alpha^5)$ term:

$$h_5 = \int_{\mathbb{R}^3} (\hat{\mathbf{u}}_1 + \hat{\mathbf{u}}_2 + \hat{\mathbf{u}}_3) \cdot [(\bar{\mathbf{u}}_\gamma + \bar{\mathbf{u}}_\delta) \cdot \nabla \mathbf{u}_1^{(0)} + \mathbf{u}_1^{(0)} \cdot \nabla (\bar{\mathbf{u}}_\gamma + \bar{\mathbf{u}}_\delta)] dv. \tag{D 6}$$

These integrals are evaluated in § 4.3.

D.2. Outer integral

The outer integral is expressed in terms of $\mathbf{R} = \alpha \mathbf{r}$. We arrange our functions in order of magnitude in α as shown below. For the $O(\alpha^4)$ term in the outer integral, we need to collect terms of $\mathbf{U}_i^{(0)}$, $\hat{\mathbf{U}}_i$ and $\bar{\mathbf{U}}$ that combine to give $O(\alpha^4)$ in the integrand of (4.8). For the $O(\alpha^5)$ term, we need an $O(\alpha^5)$ integrand in (4.8).

The leading terms in magnitude α of the $\mathbf{U}_i^{(0)}$ are

$$\mathbf{U}_1^{(0)} \sim \alpha^3 \left(\frac{1}{R^2} \mathbf{f}_1^1 + \frac{1}{R^4} \mathbf{f}_3^1 \right) + O(\alpha^4), \tag{D 7a}$$

$$\mathbf{U}_2^{(0)} \sim \alpha^3 \mathcal{S} \left[\frac{1}{R^2} \mathbf{f}_1^1 \right] + O(\alpha^4), \tag{D 7b}$$

and $\mathbf{U}_3^{(0)}$ and $\mathbf{U}_4^{(0)}$ are $O(\alpha^4)$. The leading terms in magnitude α of the $\hat{\mathbf{U}}_i$ are

$$\hat{\mathbf{U}}_1 \sim \alpha \frac{1}{R} \mathbf{g}_0^1 + \alpha^3 \frac{1}{R^3} \mathbf{g}_2^1, \tag{D 8a}$$

$$\hat{\mathbf{U}}_2 \sim \alpha \mathcal{S} \left[\frac{1}{R} \mathbf{g}_0^1 \right] + O(\alpha^3), \tag{D 8b}$$

$$\hat{\mathbf{U}}_3 \sim \alpha^2 \frac{1}{R} \mathbf{g}_0^3 + \alpha^4 \frac{1}{R^3} \mathbf{g}_2^3 + O(\alpha^4), \tag{D 8c}$$

$$\hat{\mathbf{U}}_4 \sim \alpha^2 \mathcal{S} \left[\frac{1}{R} \mathbf{g}_0^3 \right] + O(\alpha^4), \tag{D 8d}$$

while all the terms of $\bar{\mathbf{U}}$ are $O(1)$. Recall that the outer integral has the α expansion:

$$F_{L_2} = \rho U_m^2 \ell^2 (k_4 \alpha^4 + k_5 \alpha^5 + \dots). \tag{D 9}$$

Only $\mathbf{U}_1^{(0)}$, $\mathbf{U}_2^{(0)}$, $\hat{\mathbf{U}}_1$, $\hat{\mathbf{U}}_2$ and $\bar{\mathbf{U}}$ contribute to the $O(\alpha^4)$ term in the outer integral, namely,

$$k_4 = \int_{V_C} (\hat{\mathbf{U}}_1 + \hat{\mathbf{U}}_2) \cdot [\bar{\mathbf{U}} \cdot \nabla (\mathbf{U}_1^{(0)} + \mathbf{U}_2^{(0)}) + (\mathbf{U}_1^{(0)} + \mathbf{U}_2^{(0)}) \cdot \nabla \bar{\mathbf{U}}] dv, \tag{D 10}$$

whereas $\mathbf{U}_1^{(0)}$, $\mathbf{U}_2^{(0)}$, $\hat{\mathbf{U}}_3$, $\hat{\mathbf{U}}_4$ and $\bar{\mathbf{U}}$ contribute to the $O(\alpha^5)$ term:

$$k_5 = \int_{V_C} (\hat{\mathbf{U}}_3 + \hat{\mathbf{U}}_4) \cdot [\bar{\mathbf{U}} \cdot \nabla (\mathbf{U}_1^{(0)} + \mathbf{U}_2^{(0)}) + (\mathbf{U}_1^{(0)} + \mathbf{U}_2^{(0)}) \cdot \nabla \bar{\mathbf{U}}] dv. \tag{D 11}$$

These integrals are evaluated in § 4.4.

REFERENCES

- ASMOLOV, E. S. 1999 The inertial lift on a spherical particle in a plane Poiseuille flow at large channel Reynolds number. *J. Fluid Mech.* **381**, 63–87.
- BATCHELOR, G. K. 1967 *An Introduction to Fluid Dynamics*. Cambridge University Press.
- BRAMBLE, J. H. 1981 The Lagrange multiplier method for Dirichlet's problem. *Maths Comput.* **37** (155), 1–11.
- BREHERTON, F. P. 1962 The motion of rigid particles in a shear flow at low Reynolds number. *J. Fluid Mech.* **14**, 284–304.
- CHUNG, A. J., GOSSETT, D. R. & DI CARLO, D. 2013 Three dimensional, sheathless, and high-throughput microparticle inertial focusing through geometry-induced secondary flows. *Small* **9** (5), 685–690.
- COX, R. G. & BRENNER, H. 1968 The lateral migration of solid particles in Poiseuille flow – I. Theory. *Chem. Engng Sci.* **23** (2), 147–173.
- COX, R. G. & HSU, S. K. 1977 The lateral migration of solid particles in a laminar flow near a plane. *Intl J. Multiphase Flow* **3** (3), 201–222.
- DENNIS, S. C. R. & WALKER, J. D. A. 1971 Calculation of the steady flow past a sphere at low and moderate Reynolds numbers. *J. Fluid Mech.* **48** (4), 771–789.
- DI CARLO, D., EDD, J. F., HUMPHRY, K. J., STONE, H. A. & TONER, M. 2009 Particle segregation and dynamics in confined flows. *Phys. Rev. Lett.* **102** (9), 094503.
- HAPPEL, J. & BRENNER, H. 1982 *Low Reynolds Number Hydrodynamics: With Special Applications to Particulate Media. (Mechanics of Fluids and Transport Processes 1)*, Springer.
- HINCH, E. J. 1991 *Perturbation Methods. (Cambridge Texts in Applied Mathematics 6)*, Cambridge University Press.
- HO, B. P. & LEAL, L. G. 1974 Inertial migration of rigid spheres in two-dimensional unidirectional flows. *J. Fluid Mech.* **65**, 365–400.
- HOGG, A. J. 1994 The inertial migration of non-neutrally buoyant spherical particles in two-dimensional shear flows. *J. Fluid Mech.* **272**, 285–318.
- HUMPHRY, K. J., KULKARNI, P. M., WEITZ, D. A., MORRIS, J. F. & STONE, H. A. 2010 Axial and lateral particle ordering in finite Reynolds number channel flows. *Phys. Fluids* **22**, 081703.
- HUR, S. C., TSE, H. T. K. & DI CARLO, D. 2010 Sheathless inertial cell ordering for extreme throughput flow cytometry. *Lab on a Chip* **10**, 274–280.
- KIM, S. & KARRILA, S. J. 2005 *Microhydrodynamics: Principles and Selected Applications*. Dover.
- LAMB, H. 1945 *Hydrodynamics*. Dover.
- LEAL, L. G. 1980 Particle motions in a viscous fluid. *Annu. Rev. Fluid Mech.* **12** (1), 435–476.
- LECLAIR, B. P., HAMIELEC, A. E., PRUPPACHER, H. R. & HALL, W. D. 1972 A theoretical and experimental study of the internal circulation in water drops falling at terminal velocity in air. *J. Atmos. Sci.* **29** (4), 728–740.
- LEE, W., AMINI, H., STONE, H. A. & DI CARLO, D. 2010 Dynamic self-assembly and control of microfluidic particle crystals. *Proc. Natl Acad. Sci. USA* **107** (52), 22413–22418.
- MACH, A. J., KIM, J. H., ARSHI, A., HUR, S. C. & DI CARLO, D. 2011 Automated cellular sample preparation using a centrifuge-on-a-chip. *Lab on a Chip* **11**, 2827–2834.
- MAXWORTHY, T. 1965 Accurate measurements of sphere drag at low Reynolds numbers. *J. Fluid Mech.* **23**, 369–372.
- MCLAUGHLIN, J. B. 1991 Inertial migration of a small sphere in linear shear flows. *J. Fluid Mech.* **224**, 261–274.
- PAPANASTASIOU, T. C., GEORGIU, G. C. & ALEXANDROU, A. N. 1999 *Viscous Fluid Flow*. CRC Press.
- PERRY, R. 1950 *Chemical Engineers' Handbook*, 3rd edn. McGraw-Hill Education.
- RUBINOW, S. I. & KELLER, J. B. 1961 The transverse force on a spinning sphere moving in a viscous fluid. *J. Fluid Mech.* **11**, 447–459.
- SAFFMAN, P. G. 1965 The lift on a small sphere in a slow shear flow. *J. Fluid Mech.* **22**, 385–400.
- SCHONBERG, J. A. & HINCH, E. J. 1989 Inertial migration of a sphere in Poiseuille flow. *J. Fluid Mech.* **203**, 517–524.

- SEGRÉ, G. & SILBERBERG, A. 1961 Radial particle displacements in Poiseuille flow of suspensions. *Nature* **189** (4760), 209–210.
- SEGRÉ, G. & SILBERBERG, A. 1962a Behaviour of macroscopic rigid spheres in Poiseuille flow. Part 1. Determination of local concentration by statistical analysis of particle passages through crossed light beams. *J. Fluid Mech.* **14**, 115–135.
- SEGRÉ, G. & SILBERBERG, A. 1962b Behaviour of macroscopic rigid spheres in Poiseuille flow. Part 2. Experimental results and interpretation. *J. Fluid Mech.* **14**, 136–157.
- SOLLIER, E., GO, D. E., CHE, J., GOSSETT, D. R., O'BYRNE, S., WEAVER, W. M., KUMMER, N., RETTIG, M., GOLDMAN, J., NICKOLS, N., MCCLOSKEY, S., KULKARNI, R. P. & DI CARLO, D. 2014 Size-selective collection of circulating tumor cells using vortex technology. *Lab on a Chip* **14**, 63–77.
- VASSEUR, P. & COX, R. G. 1976 The lateral migration of a spherical particle in two-dimensional shear flows. *J. Fluid Mech.* **78**, 385–413.
- VEYSEY, J. & GOLDENFELD, N. 2007 Simple viscous flows: from boundary layers to the renormalization group. *Rev. Mod. Phys.* **79**, 883–927.